

Amending the Anisotropy Barrier and Luminescence Behavior of Heterometallic Trinuclear Linear $[M_{II}-Ln_{III}-M_{II}]$ ($Ln_{III} = Gd, Tb, Dy$; $M_{II} = Mg / Zn$) Complexes by Change from Divalent Paramagnetic to Diamagnetic Metal ions

Sourav Das,^[a] K. S. Bejoymohandas,^{[b], [c]} Atanu Dey,^[a] Sourav Biswas,^[a] M. L. P. Reddy,^{[b], [c]}

Roser Morales^[d], Eliseo Ruiz^[d], Silvia Titos-Padilla,^[e] Enrique Colacio,^{*, [e]} and Vadapalli

Chandrasekhar,^{*, [a], [f]}

[a] Department of Chemistry, Indian Institute of Technology Kanpur, Kanpur-208016, India

Home page: <http://www.iitk.ac.in>

[b] Materials Science and Technology Division, National Institute for Interdisciplinary Science and Technology (NIIST), Council of Scientific and Industrial Research (CSIR), Thiruvananthapuram 695 019, India.

Home page: <http://www.niist.res.in/english/>

[c] Academy of Scientific and Innovative Research (AcSIR), New Delhi 110001, India.

Home page: <http://acsir.res.in/>

[d] Departament de Química Inorgànica and Institut de Recerca de Química Teòrica i Computacional, Universitat de Barcelona, Diagonal 645, E-08028 Barcelona, Spain

[e] Departamento de Química Inorgánica, Facultad de Ciencias, Universidad de Granada, Avenida de Fuentenueva s/n, 18071 Granada, Spain.

Home page: <http://www.ugr.es>

[f] National Institute of Science Education and Research, Institute of Physics Campus, SachivalayaMarg, PO: Sainik School, Bhubaneswar - 751 005, India.

Abstract

The sequential reaction of a multisite coordinating compartmental ligand LH₄ [2-(2-hydroxy-3-(hydroxymethyl)-5-methylbenzylideneamino)-2-methylpropane-1,3-diol] with appropriate lanthanide salts followed by the addition of Mg(NO₃)₂·6H₂O or Zn(NO₃)₂·6H₂O in a 4:1:2 stoichiometric ratio in the presence of triethylamine affords a series of isostructural heterometallic trinuclear complexes containing [Mg₂Ln]₃₊ [Ln = Dy (**1**), Gd (**2**) and Tb (**3**)] and [Zn₂Ln]₃₊ [Ln = Dy (**4**), Gd (**5**) and Tb (**6**)] cores. The formation of **1-6** is demonstrated by X-ray crystallography as well as ESI-MS spectra. All complexes are isostructural possessing a linear trimetallic core with a central lanthanide ion. In this article we have discussed the comprehensive studies, involving synthesis, structure, magnetism and photophysical properties on this family of trinuclear [Mg₂Ln]₃₊ and [Zn₂Ln]₃₊ heterometallic complexes. Complexes **1** and **4** show slow relaxation of the magnetization below 12 K under zero applied direct-current field, but without reaching a neat maximum which is due to the overlapping with a faster quantum tunnelling relaxation mediated through dipole-dipole and hyperfine interactions. Under a small applied direct-current field of 1000 Oe the quantum tunneling was almost suppressed and temperature and frequency dependent peaks were observed, thus confirming the SMM behavior of complexes **1** and **4**. The fit of the high-temperature relaxation times to the Arrhenius equation affords an effective energy barrier for the reversal of the magnetization of $U_{\text{eff}} = 72(2)$ K with $\tau_0 = 8 \times 10^{-9}$ s for the SR process and $U_{\text{eff}} = 61(2)$ K with $\tau_0 = 4 \times 10^{-7}$ s for the FR process for **1** whereas for **4**,

an effective energy barrier for the reversal of the magnetization $U_{\text{eff}} = 67(3)$ K with $\tau_0 = 4.5 \times 10^{-8}$ s. To rule out the involvement of intermolecular collaborative interactions in the dynamic of relaxation, we have performed *ac* susceptibility measurements on 1:10 Dy:Y magnetic diluted samples of **1** and **4**, named as **1'** and **4'**. Interestingly, the diluted compounds **1'** and **4'** exhibits SMM behavior under zero magnetic field, thus suggesting that their relaxation processes are single molecular in origin and arise from the M-Dy-M unit. Ab initio CASSCF+RASSI calculations carried out on **1** and **4** confirm that the magnetic anisotropy is axial along the M-Dy-M axis and that the relaxation process occurs through the first excited energy level. Furthermore, the chromophoric [LH₃]₂⁻ ligand is able to act as an “*antenna*” group which was found to be effective in the selective sensitization of the emissions of Tb^{III}-based complexes **3** and **6**. The emission quantum yields and the luminescence lifetimes at room temperature are 11.7 % and 0.606 ms for **3**, 22.7 % and 0.799 ms for **6**.

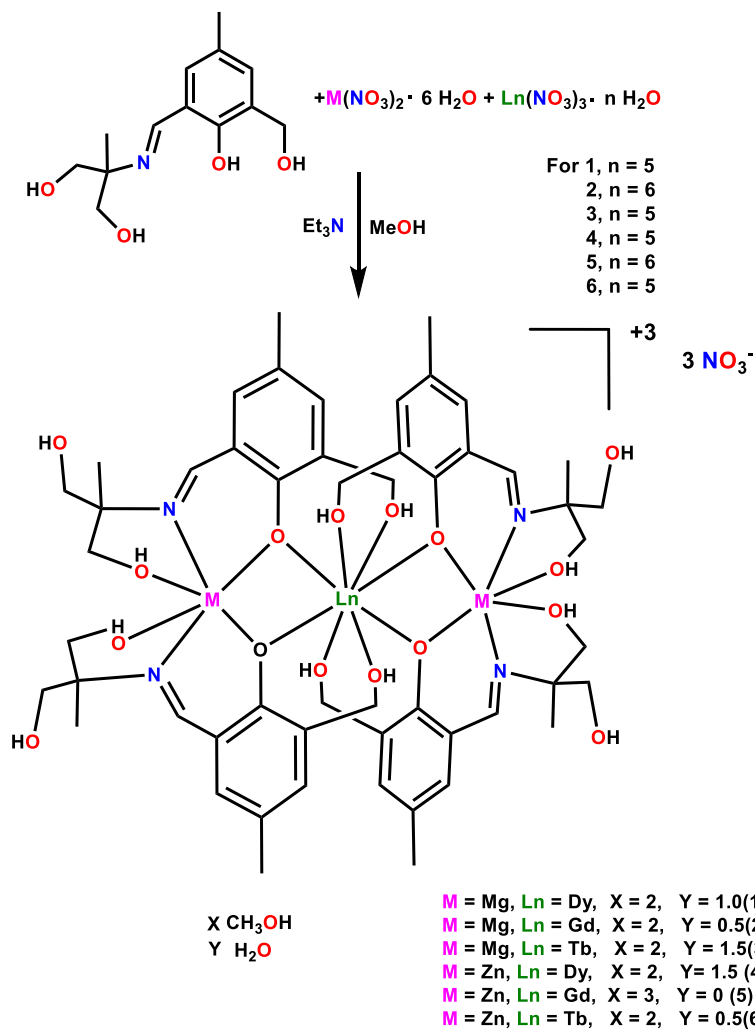
Keywords: Coordination Chemistry; Heterometallic complexes; Magnetic properties; Single molecule magnet behaviour, Photoluminescence properties.

Introduction

Coordination compounds involving lanthanide metal ions have been attracting interest in view of their potential ability to behave as single-molecule magnets, which have been proposed for applications in molecular spintronics,[1] ultrahigh density magnetic information storage,[2] and quantum computing[3]. The utility of the lanthanide ions is due to the fact that some of them have large unquenched orbital angular momenta and consequently large intrinsic magnetic anisotropy besides carrying a significant magnetic moment (i.e., Dy^{III}, Tb^{III}, Ho^{III}, Er^{III}). In spite of the attractiveness of lanthanide ion complexes in single-molecule magnets,[4] it is to be noted that fast quantum tunnelling mechanism (QTM)-induced relaxation processes mediated through dipolar interactions, transverse anisotropy, or hyperfine interactions can reduce the energy barrier to an effective value (U_{eff}), thus diminishing the SMM properties of the lanthanide-containing species.[5] To overcome this, there are a few techniques such as the dilution of such complexes within a diamagnetic matrix to eliminate dipolar interactions[6] and/or the application of a small static magnetic field[7] to partly or fully suppress the QTM relaxation processes. We, [8] and others,[9] have experimentally shown that the very weak $J_{\text{M-Ln}}$ value observed for 3d/4f dinuclear ($\text{M}_{\text{II}} = \text{Mn, Co, Ni, and Cu}$) [8c-e] and trinuclear ($\text{M}_{\text{II}} = \text{Co and Ni}$) [8a], [8b] complexes display small effective energy barriers for the separations of the low-lying split sublevels and consequently to a smaller energy barrier for magnetization flipping. In this regard, an effective plan to boost the SMM properties of the 3d/4f aggregates would be get rid of the very weak $\text{M}_{\text{II}}\text{--Ln}_{\text{III}}$ interactions that split the ground sublevels of the Ln_{III} ion by substituting the paramagnetic M_{II} ions by a diamagnetic ion [6c], [9a], [10]. In addition to their interest in magnetism, lanthanide complexes are also of interest in photoluminescence with potential applications ranging from

biomedical analysis^[11] (fluoroimmuno assays, cellular imaging, and MRI contrast agents) to materials science (tunable lasers, amplifiers for optical communications, optical fibers, light emitting diodes etc). ^[12] These applications are possible because of some important characteristics of the lanthanide ions: long excited-state life times, high-quantum efficiencies, substantial Stokes shifts and sharp line-like emission bands ranging from near infra-red (Pr^{III}, Nd^{III}, Er^{III}) to visible (Eu^{III}, Tb^{III}) spectral domains.^[13] In spite of these favourable physical properties, direct photoexcitation of lanthanide ions has some intrinsic drawbacks as a result of spin and parity forbidden *f-f* transition.^[14] One of the ways of overcoming this problem is to use suitable organic ligands as sensitizers/chromophores. The latter not only can shield the lanthanide ions from vibrational coupling, but also, under favourable conditions, transfer energy to the lanthanide centre via the so called *antenna* effect.^[15] In addition to this well-known strategy, more recently there has been interest on 3d-4f complexes, where the 3d-metal complex moiety can act as the antenna chromophore for sensitization of lanthanide ions.^[16] Several ongoing efforts reveal that near-UV or visible range absorbing d-block metal complexes can function as low-energy sensitizers resulting in a strong/bright emission from the d/f ensemble.^[16] On the other hand, utilization of s/f heterometallic combinations have not received attention. Previously, utilizing a tris-hydrazone ligand, P(S)[N(CH₃)N=CHC₆H₄-o-OH]₃ (LH₃), we constructed trinuclear Mg(II) complexes that showed promising luminescent properties^[17]. Also, this ligand system and its variation were used to prepare 3d and 3d/4f complexes^[18]. In view of this we are interested to assemble hetero-bimetallic complexes of the type Mg^{II}/Ln^{III} and Zn^{II}/Ln^{III} with a view to probe their magnetism and photophysical properties. Accordingly, we report the first comprehensive studies, involving synthesis, structure, magnetism and

photophysical properties on a family of trinuclear $[\text{Mg}_2\text{Ln}]^{3+}$ and $[\text{Zn}_2\text{Ln}]^{3+}$ heterometallic complexes.

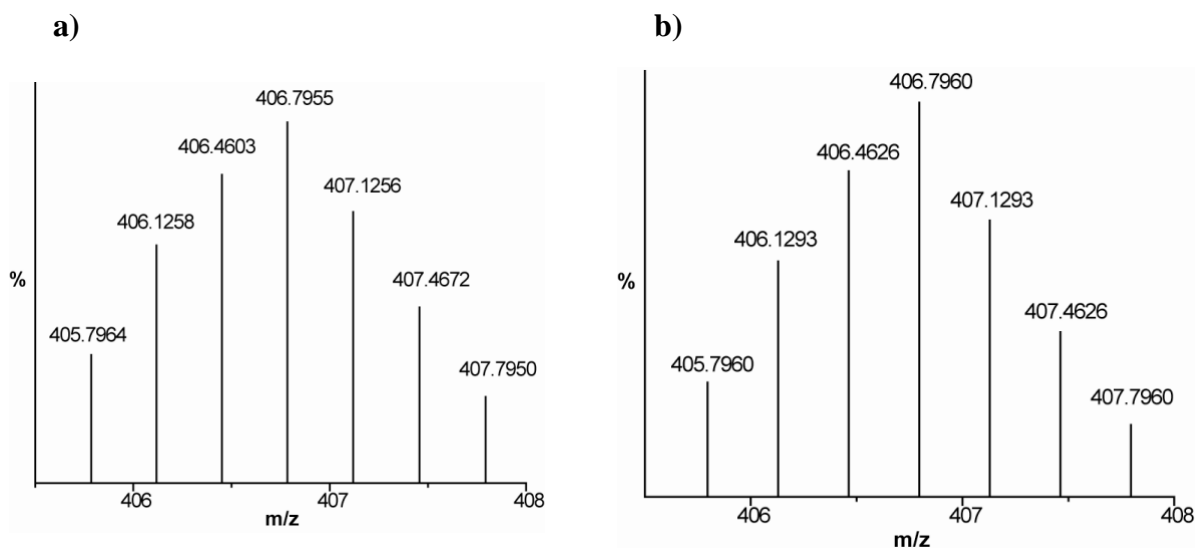


Scheme 1. Synthesis of the trinuclear heterometallic complexes **1-6**.

Results and Discussion

Synthetic Aspects

We have recently reported the efficacy of the ligand 2-(2-hydroxy-3-(hydroxymethyl)-5-methylbenzylideneamino)-2-methylpropane-1,3-diol (LH₄) to assemble a series of linear trinuclear heterometallic Co_{II}Ln (Ln = Gd, Tb, Dy and Ho) [8b] as well as Ni_{II}Ln [8a] (Ln = Gd, Tb, Dy and Ho) complexes. Spurred by these results, we were interested in examining the generality of LH₄ in assisting such heterometallic ensembles. Accordingly, the sequential reaction of LH₄ with Ln(NO₃)₃·nH₂O, followed by the addition of Mg(NO₃)₂·6H₂O/Zn(NO₃)₂·6H₂O in a 4:1:2 stoichiometric ratio in the presence of triethylamine afforded a series of isostructural heterometallic trinuclear complexes containing [Mg₂Ln]₃⁺ [Ln = Dy (**1**), Gd (**2**) and Tb(**3**)] and [Zn₂Ln]₃⁺ [Ln = Dy (**4**), Gd (**5**) and Tb (**6**)] cores (Scheme 1). ESI-MS spectra of **1-6** reveal that they retain their molecular integrity in solution (see experimental section and Supporting Information). The ESI-MS spectrum of **1**, as a representative example, is given in Figure 1 while those of the others are given in the Supporting Information (Figures S1-S5).



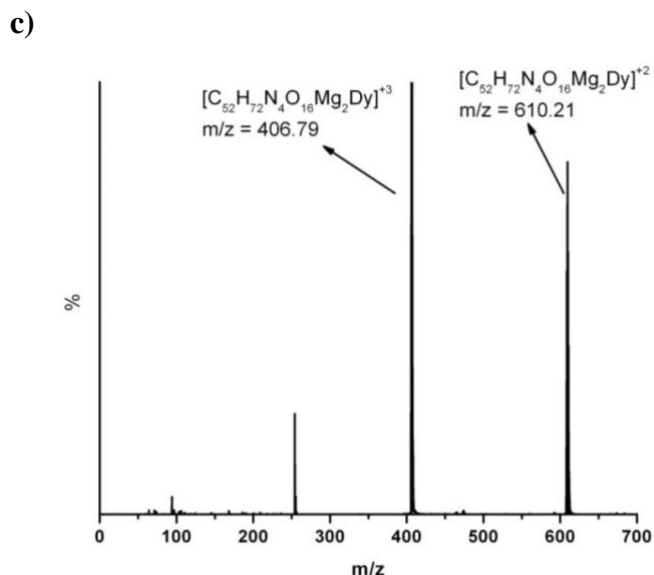


Figure 1. (a) Experimental mass spectral pattern of the parent ion peak of complex **1**; (b) simulated isotopic pattern for the parent ion peak showing a close resemblance with the experimental spectrum and (c) full range ESI-MS spectrum of complex **1**.

Molecular Structures of 1-6

Single-crystal X-ray diffraction studies reveal that complexes **1-6** are isostructural (only with the change in the divalent metal ions; Mg^{II} in complexes **1-3** and Zn^{II} in complexes **4-6**) and crystallize in the monoclinic space group $P2_1/n$. Complexes **1-6** are tricationic, containing three nitrates as the counter anions.

The molecular structure of **1** will be discussed herein to illustrate the common structural features of the six complexes. The molecular structure of **1** is shown in Figure 2 and those of **2-6** are given in Supporting Information (Figure S6). Bond parameters associated with complex **1** are

given in the caption of Figure 2 and those of complexes **2-6** are given in the Supporting information (Tables S1 to S5 respectively).

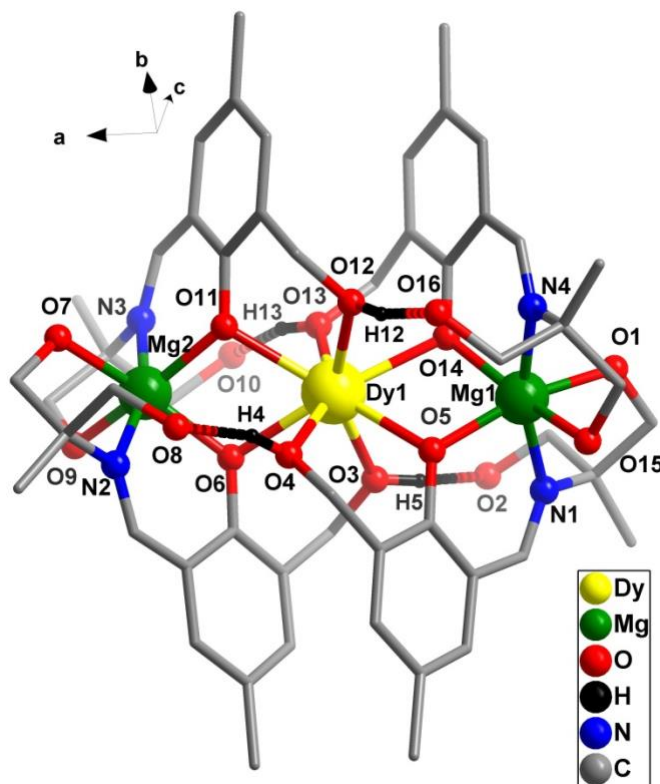


Figure 2. The tricationic complex, **1** (hydrogen atoms, the solvent molecules and nitrate counter anion have been omitted for clarity). Selected bond distance (Å) and bond angle (°) parameters: Dy(1)-O(3) 2.329(5), Dy(1)-O(11) 2.346(5), Dy(1)-O(6) 2.353(5), Dy(1)-O(14) 2.354(6), Dy(1)-O(5) 2.383(6), Dy(1)-O(4) 2.395(7), Dy(1)-O(13) 2.407(7), Dy(1)-O(12) 2.411(6), Dy(1)-Mg(2) 3.482(3), Dy(1)-Mg(1) 3.484(3), Mg(1)-O(3) 1.989(7), Mg(1)-O(14) 2.031(7), Mg(1)-O(1) 2.062(10), Mg(1)-N(4) 2.106(9), Mg(1)-O(15) 2.124(9), Mg(1)-N(1) 2.154(8), Mg(2)-O(6) 1.994(6), Mg(2)-O(11) 2.016(6), Mg(2)-O(9) 2.078(7), Mg(2)-O(7) 2.108(7), Mg(2)-N(2) 2.126(8), Mg(2)-N(3) 2.144(9), Mg(1)-O(3)-Dy(1) 107.3(3), Mg(2)-O(6)-Dy(1) 106.2(2), Mg(2)-O(11)-Dy(1) 105.7(2), Mg(1)-O(14)-Dy(1) 105.0(3).

The heterometallic complexes are formed by the cumulative coordination action of four [LH₃]⁻ ligands. Although the ligand LH₄ consists of four coordination sites that can lose a proton, under the reaction conditions only the phenolic proton gets deprotonated. This phenomenon is similar to that observed in our previous reports.⁷ The assembly of the trinuclear complexes can be described in the following way. The phenolate oxygen of each ligand LH₄ adopts a μ -bridge between the Mg^{II} and the lanthanide ion. The bond distances associated with the phenolate oxygen and the metal centers are as follows: Mg–O_{avg}~ 2.008 Å and Dy–O_{avg}~ 2.345 Å. Due to the participation of four [LH₃]⁻ in coordination, two four-membered rings (Mg1-O3-Dy1-O14 and Mg2-O6-Dy-O11) are generated (Figure 3).

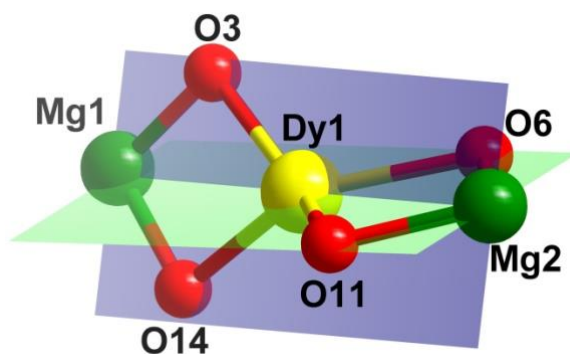


Figure 3. The trinuclear core of **1** showing two four-membered MgDyO₂ rings at an angle of ~ 60°.

The two four-membered rings bisect each other with an angle of 59.7°. Some more details of the coordination behaviour are as follows. The imino-nitrogen of the ligand binds with Mg^{II} ion with a distance of 2.016–2.144 Å. The benzylic hydroxyl group of the ligand is not deprotonated and coordinates with the dysprosium ion with a distance of Dy–O_{avg}~ 2.398 Å. The alcoholic hydroxyl group of the ligand also remains protonated and one alcoholic hydroxyl group

coordinates with the Mg^{II} ion with a distance of 2.062–2.124 Å. The other protonated alcoholic hydroxyl group remains free and takes part in an intramolecular hydrogen bonding with the benzylic hydroxyl group (Figure 2). Further, a two-dimensional hydrogen bonding network is seen along the *ab* plane; each trinuclear unit interacts with four neighbouring molecules through the nitrate anions (Figure S7). The bond parameters associated with the intra and inter molecular hydrogen bonding are given in Table S6. Based on the various coordination actions as discussed above, Mg^{II} ion is hexacoordinated (2N, 4O), in a distorted octahedral geometry; Dy^{III} ion is eight coordinated (8O) and in a distorted square antiprismatic geometry (Figure 4). Within the DyO₈ square antiprism, the interplanar distance, d_{pp} (distance between the upper and lower planes comprising four oxygen atoms: O3, O4, O5, O6 and O11, O12, O13, O14) is 2.539 Å, whereas the intraplanar distances d_{ip} (the shortest distance between the oxygen atoms defining the above indicated planes) is 2.840 Å. The d_{pp} and d_{ip} values clearly indicate an axial compression of the square-antiprism in **1**.^[5d] Besides this, the α angle (angle between the S8 axis, which is almost perpendicular to the M-Dy-M axis, and a Dy-O direction) of 60.81° is greater than the magic angle $\alpha = 57.4^\circ$ (angle for non-distorted square antiprism) ^[5b] also supports the axial compression phenomena of the square-antiprism in **1**. The angle between the diagonals of the two squares, φ (skew angle), is 55.24° (for the ideal square antiprism geometry φ is 45°) whereas the dihedral angle between the upper and lower O4 squares is $\theta = 1.2^\circ$ (the ideal geometry θ angle is zero). The values of the above structural parameters (d_{ip} , d_{pp} , α , φ , θ) point to a rather distorted DyO₈ square antiprism. In connection with this, the calculation of the degree of distortion of the DyO₈ coordination polyhedron with respect to an ideal eight-vertex polyhedra, by using the continuous shape measure theory and SHAPE software^[19], show that the DyO₈ arrangement is intermediate between various coordination polyhedral (Tables S7). The

lowest shape measures correspond to square antiprism (SAPR-8), biaugmented trigonal prism (BTPR-8) and trigonal dodecahedron (TDD-8) with values of 1.113, 2.166 and 2.196, respectively. The structural parameters and shape measures for **4** are very close to those found for **1** (Table S8).

The three metal centres are arranged in a linear fashion with an intermetallic Mg1–Dy–Mg2 angle of 177.9°. The intermetallic separations are in the range of Mg–Dy = 3.48 Å and Mg–Mg = 6.96 Å.

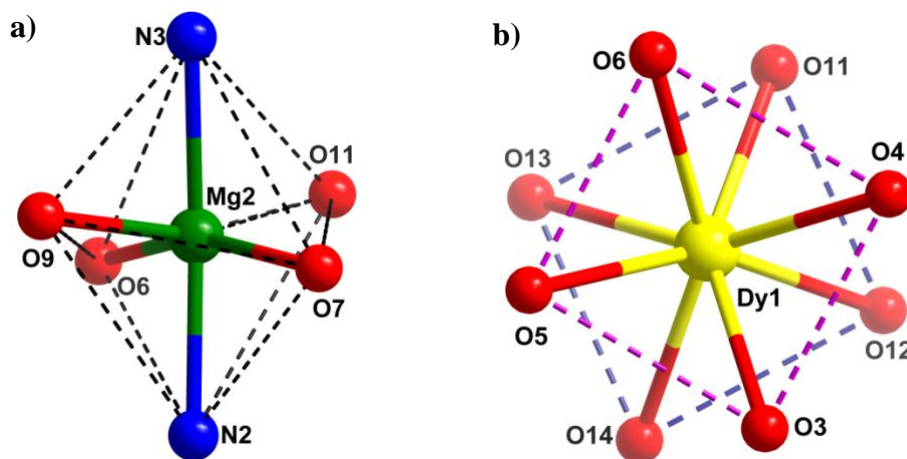


Figure 4. (a) Distorted octahedral geometry around Mg(II) ion and (b) distorted square-antiprismatic geometry around Dy(III) ion.

Magnetic properties

The direct-current (*dc*) magnetic susceptibilities (χ_M) of complexes **1-6** has been measured in the 2-300 K temperature range under an applied magnetic field of 0.1 T and are given in Figure 5 in the form $\chi_M T$ vs T .

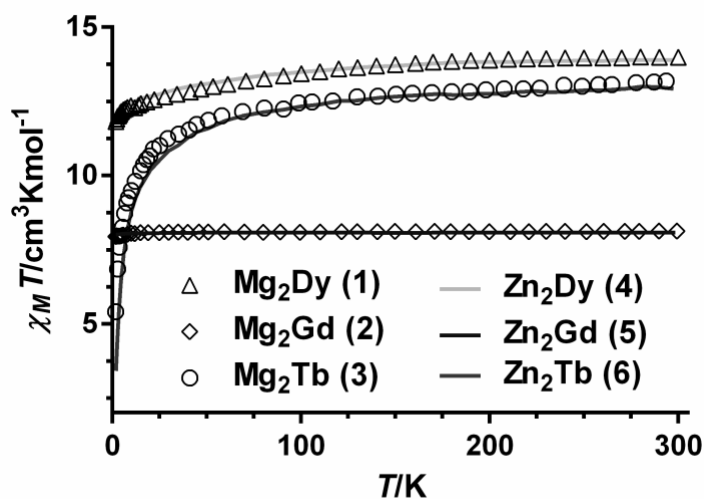


Figure 5. Temperature dependence of the $\chi_M T$ for complexes **1-6**.

The room temperature $\chi_M T$ values for these complexes are very close to those calculated for isolated Ln^{III} ions in the free-ion approximation (Table 1).

Table 1: Direct current magnetic data for **1-6**.

Compound	Ground state of the Ln^{3+} ion	$\chi_M T$ theoretical ^a / at 300 K (experimental)/ at 2K (experimental) ($\text{cm}^3 \text{K mol}^{-1}$)	Calculated saturation value ^b μ_B at 2 K and 5 T ($N\mu_B$)
1		14.17/13.99/11.82	10/5.08

4	${}^6H_{15/2}, g_J=4/3$	14.17/13.90/12.08	10/5.23
2	${}^8S_{7/2}, g_J=2$	7.875/8.125/7.944	7.0/7.04
5		7.875/8.07/8.01	7.0/7.15
3	${}^7F_6, g_J=3/2$	11.82/13.18/5.41	9.0/5.49
6		11.82/12.93/3.4	9.0/5.57

$$^a \chi_M T = \frac{N\beta^2}{3k} \{g_J^2 J(J+1)\} \quad ^b M = NJ\mu_B; \quad J = L + S; \quad g_J = \frac{3}{2} + \frac{S_T(S_T+1) - L(L+1)}{2J(J+1)}$$

On cooling, the $\chi_M T$ product of the Dy^{III} (**1** and **4**) and Tb^{III} (**3** and **6**) complexes steadily decreases down to 2 K, which is due to the depopulation of the excited m_j sublevels of the Dy^{III} and Tb^{III} ions, which arise from the splitting of the ${}^6H_{15/2}$ and 7F_6 ground terms, respectively, by the ligand field, and/or possible very weak intermolecular interactions between the Ln³⁺ ions. The $\chi_M T$ product for the Gd^{III} compounds (**2** and **4**) remains almost constant from room temperature to 2 K, as expected for such an isotropic ion.

The field dependence of the magnetization for complexes **1-6** are given in Figure S8. The M versus H plot at 2 K for the Dy^{III} (**1** and **4**) and Tb^{III} (**3** and **6**) complexes shows a relatively rapid increase in the magnetization at low field to reach almost saturation for magnetic fields of 5T. The observed saturation values for the Dy^{III} and Tb^{III} complexes are rather lower than the calculated ones, which is due to crystal-field effects leading to significant magnetic anisotropy.^{[7a], [20]}

The relatively simple point-charge model ^[5b, 5d] predicts just that DyO₈ coordination environments with an axially elongated square-antiprism D_{4d} symmetry, which can be achieved by increasing the electronic density near to the S₈ axis, favor the SMM behavior. On the other hand, the axially

compressed square-antiprism D_{4d} symmetry, which can be reached by increasing the electronic density near to the basal plane, does not favour the SMM behavior in DyO_8 complexes but in the Er_{3+} counterparts. Taking into account exclusively the above symmetry criterion, compounds **1** and **4**, both possessing axially compressed square-antiprism D_{4d} symmetry, should not exhibit SMM behavior. It is worth mentioning that this symmetry criterion applies quite well to homoleptic DyO_8 systems with almost equivalent oxygen atoms. However, in heteroleptic DyO_8 systems with distorted square-antiprism D_{4d} symmetry and non-equivalent oxygen atoms, the symmetry criterion is unsuitable for predicting SMM behavior. In these cases, the differences in charge between the oxygen atoms coordinated to the Dy_{3+} ion play a central role in dictating the SMM behavior. In this regard, the free ion electron density for the Dy_{III} ion has an oblate shape, which can be stabilized by an axial crystal field, where the donor atoms with the largest electron densities are located above and below the equatorial plane, thus minimizing the repulsive interactions between the ligands and f -electrons charge clouds. [5c],[9a],[10e] The oxygen atoms involved in the shortest Dy-O bond distances give rise to increased electrostatic repulsions with the Dy_{3+} electron density and, to reduce these repulsive interactions, the Dy_{3+} disc surface electron density is accommodated almost perpendicular to the shortest Dy-O bonds. [4g], [10b], [10g], [21]. Therefore, the magnetic moment that is perpendicular to the electron density disc is found in the direction of the shortest Dy-O bonds. In the case of the heteroleptic complexes **1** and **4**, the shortest Dy-O distances involve the phenoxide-oxygen donor atoms at opposite positions of the Dy_{III} ion and therefore an easy-axis anisotropy could be expected, the magnetic moment lying parallel to the direction defined by the phenoxide-oxygen atoms and therefore close to the M-Dy-M ($M = Mg_{II}$ and Zn_{II}) line. The presumable easy-axis anisotropy of the Dy_{III} ion favors the slow relaxation of the magnetization and the SMM behavior.

In order to know if compounds **1-6** exhibit slow relaxation of the magnetization and SMM behavior, *ac* magnetic susceptibility measurements as a function of the temperature and frequency were performed under zero and 1000 Oe *dc* fields. The results of these measurements demonstrate that only compounds **1** and **4** exhibit frequency dependence the out-of-phase (χ''_M) signals typical of thermally activated relaxation process (Figure S9 and S10). However, no neat maxima are observed in the temperature dependence of the out-of-phase (χ''_M) at different frequencies, which can be due to overlapping of different relaxation processes, including a faster quantum tunnelling relaxation process even at frequencies as high as 1400 Hz. This behaviour seems to indicate that **1** and **4** shows slow relaxation of the magnetization and possibly SMM behaviour. The increase of the out-of-phase (χ''_M) signals at very low temperature can be taken as a clear indication of the existence of fast quantum tunneling of magnetization.

When the *ac* measurements were performed in the presence of a small external *dc* field (Figure 6) of 1000 G to fully or partly suppress the quantum tunneling relaxation of the magnetization (QTM), broad peaks appear for **1** with maxima in the temperature range 9.0 K (1488 Hz)-4.5 K (10 Hz). For frequencies upper than 280 Hz two maxima begin to be visible in the 6-9 K range. It should be mentioned that the existence of several thermally activated relaxation processes for crystallographically equivalent D_{3h} ions is not unprecedented, [4g], [7a], [9b] demonstrating once again the complexity of the relaxation processes occurring for $4f$ -containing complexes. The Cole-Cole diagram for **1** in the temperature range 5-6 K (Figure S11) exhibits semicircular shapes but the semicircles become distorted between 6.2 K and 8.2 K indicating the presence of two relaxation process. The fitting of the Cole-Cole plot to the generalized Debye model for two thermally activated processes allowed the extraction of their corresponding relaxation times.

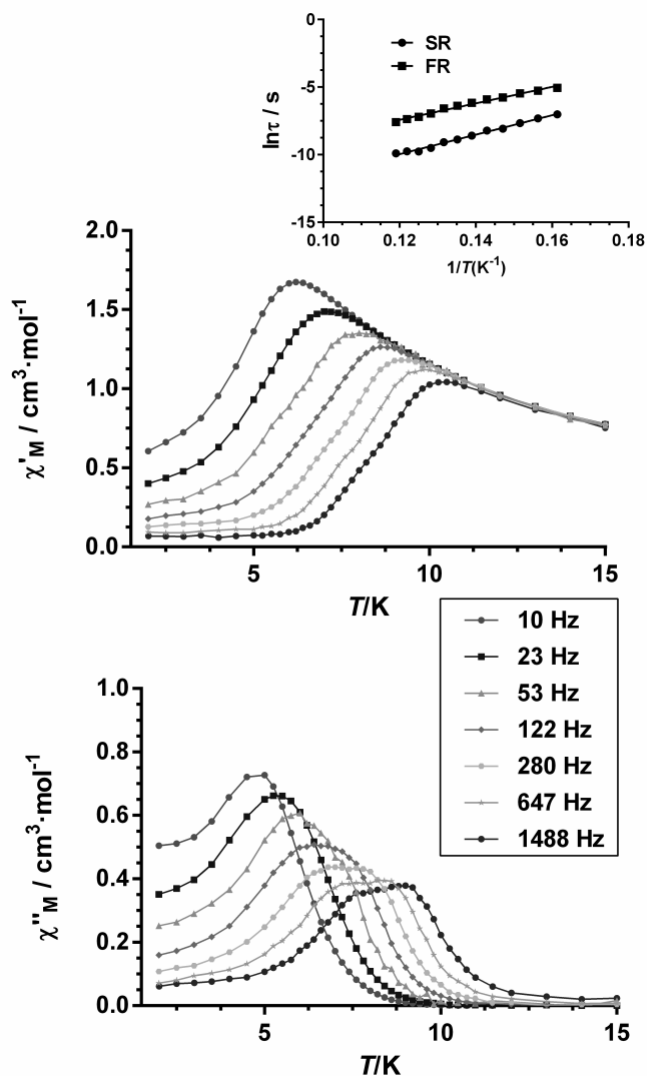


Figure 6. Temperature dependence of in-phase χ'_M (top) and out-of-phase χ''_M (bottom) components of the *ac* susceptibility for complex **1** measured under 1000 Oe applied *dc* field and Arrhenius plot (inset).

The fit of the temperature dependence of the relaxation times for both processes to the Arrhenius equation (Figure 6 inset) afforded an effective energy barrier for the reversal of the magnetization of

$U_{\text{eff}} = 72(2)$ K with $\tau_0 = 8 \times 10^{-9}$ s for the SR process and $U_{\text{eff}} = 61(2)$ K with $\tau_0 = 4 \times 10^{-7}$ s for the FR process. The Arrhenius plot constructed with the relaxation times extracted from the fitting of the χ''_{M} vs frequency data to the Debye equation for only one relaxation process leads to an intermediate value of $U_{\text{eff}} = 68(1)$ K with $\tau_0 = 7 \times 10^{-8}$ s, as expected.

AC susceptibility measurements under an external *dc* field of 1000 G for **4** (Figure 7) show that the quantum tunneling relaxation of the magnetization (QTM) is almost suppressed and maxima are observed in the temperature range 4.5 K (10 Hz)-8.0 K (1400 Hz). The Cole-Cole diagram for **4** in the temperature range 4.5-9 K (Figure S12) exhibits semicircular shapes and can be fitted using the generalized Debye model, affording α values (this parameter determines the width of the distribution of relaxation times, so that $\alpha = 1$ corresponds to an infinitely wide distribution of relaxation times, whereas $\alpha = 0$ describes a single relaxation process) in the range 0.31(4.5 K)-0.21(9 K), which suggest the existence of more than one relaxation process. The relaxation times extracted from the frequency-dependent susceptibility data follow an Arrhenius law with an effective energy barrier for the reversal of the magnetization $U_{\text{eff}} = 67(3)$ K and $\tau_0 = 4.5 \times 10^{-8}$ s (Figure 7, inset). The Arrhenius plot constructed from the temperatures and frequencies of the maxima observed for the χ''_{M} signals in Figure 7 leads virtually to the same result. As expected, the isostructural complexes **1** and **4** exhibit very similar SMM behavior with almost identical U_{eff} and τ_0 parameters.

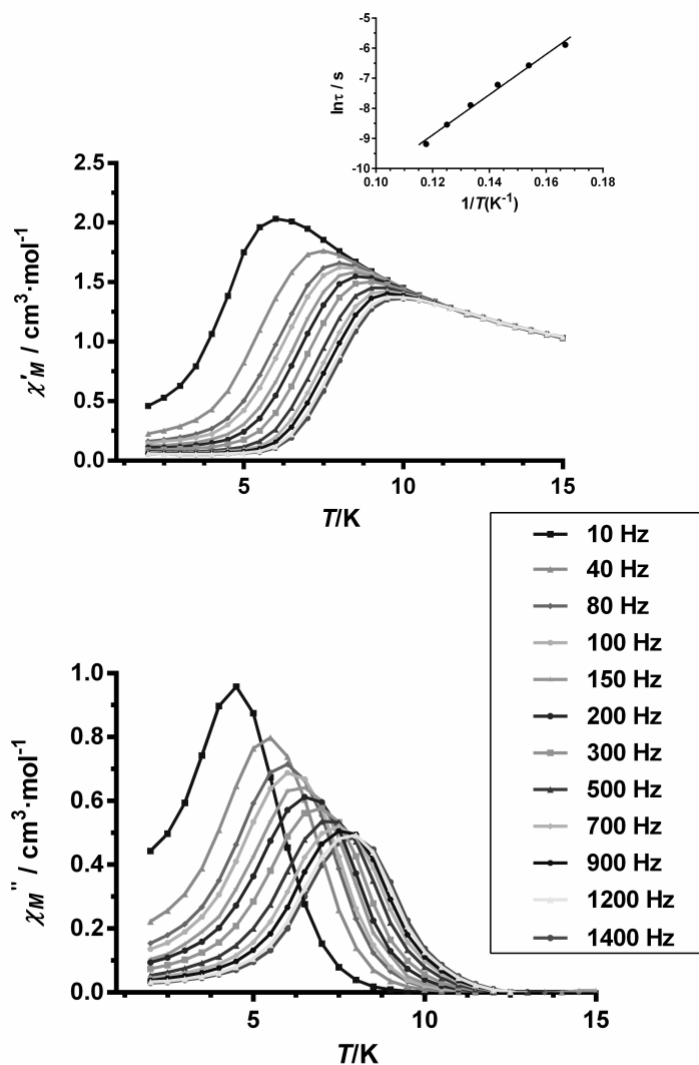


Figure 7. Temperature dependence of in-phase χ'_M (top) and out-of-phase χ''_M (bottom) components of the *ac* susceptibility for complex **4** measured under 1000 Oe applied *dc* field and Arrhenius plot (inset).

It is well known that when different processes contribute to the relaxation, the Arrhenius plot usually deviates from linearity [22]. Despite the fact that the α values extracted from **1** and **4** under a 1000 Oe static magnetic field indicate the existence of a distribution of relaxation processes, the

relaxation times for these complexes do not deviate from the Arrhenius linear plot in the temperature range where the curves corresponding to the frequency dependence of the out-of-phase signals show maxima (curves used to extract accurate relaxation times).

We have performed magnetization hysteresis loop measurements on powder samples of **1** and **4** at 2 K and using a sweeping rate of 0.25 T with the aim of confirming the SMM properties of these compounds (Figure 8 and S13). The compounds exhibit at 2 K butterfly shaped hysteresis loops with a large step near zero field, which is consistent with the QTM generally found for 4f containing complexes and with the tail that these compound exhibits at low temperature in the χ_M'' vs T plot.

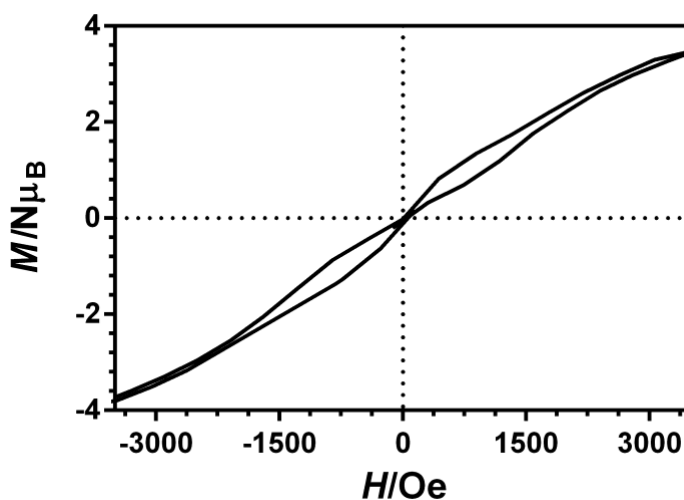


Figure 8. Magnetic hysteresis loop for **1** at 2 K and using a sweeping rate of 0.25 T.

In order to know how the intermolecular magnetic dipolar interactions influence the relaxation of the magnetization in these complexes and to unequivocally demonstrate that the relaxation process is single molecular in origin, we have performed *ac* susceptibility measurements on the

magnetic diluted samples **1'** and **4'**. These samples were prepared through crystallization with the diamagnetic and isostructural Mg_2Y and Zn_2Y complexes using a Dy/Y molar ratio of 1:10 (the amount of Dy present in the dilute sample was calculated to be 10.8 and 10.2% for **1'** and **4'**, respectively, from the magnetization values at 5 T and 2 K of the magnetic dilute and neat compounds). X-Ray powder spectra for **1'** and **4'** clearly show that these complexes are isostructural between themselves and with the neat compounds (Figure S14). Interestingly, the diluted compounds **1'** and **4'** show under zero-field (Figure S15 and Figure 9) out-of-phase peaks in the ranges 6.5 (2000)-8.5K (1000 Hz) and 6.5 (300)-8K (1400 Hz), respectively. The removal of intermolecular interactions in the diluted complex partly suppresses the QTM process and slows relaxation of the magnetization thus allowing the appearance of clear maxima in the temperature dependence of the out-of-phase (χ''_{M}) signals at different frequencies. Below approximately 5 K, the out-of-phase (χ''_{M}) signals increase and show the typical tail due to the fast quantum tunneling of magnetization in the ground state.

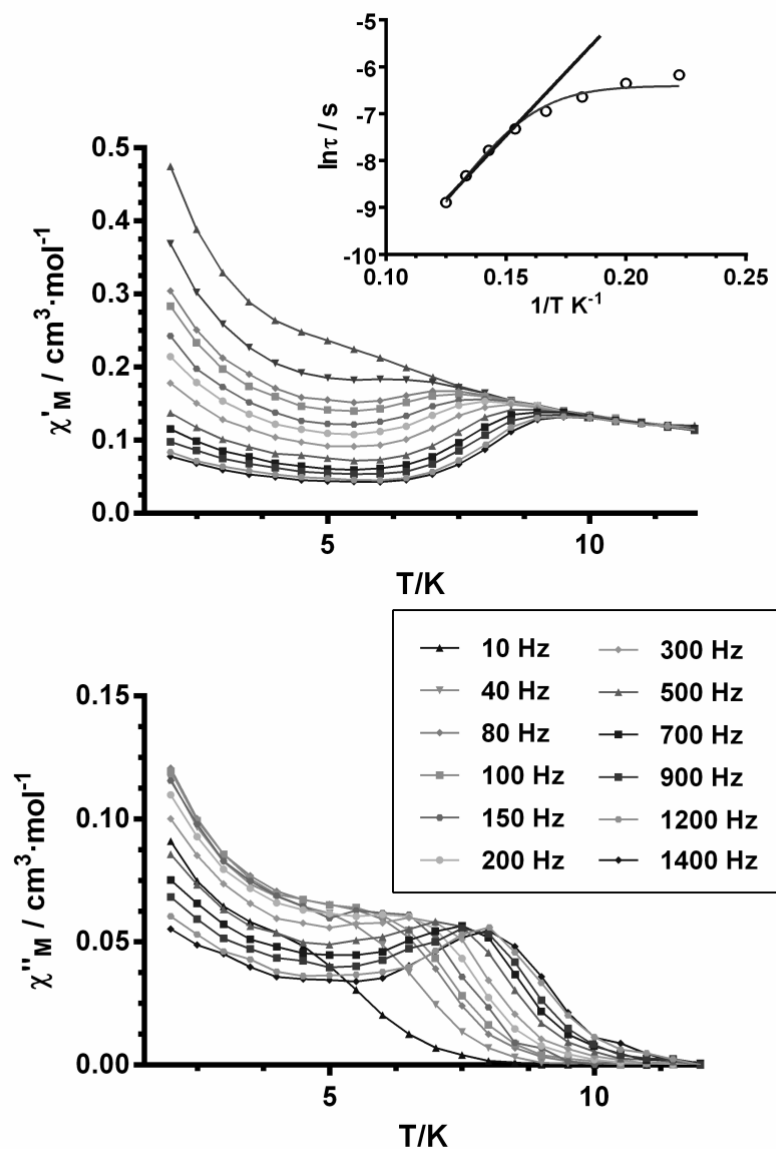


Figure 9. Temperature dependence of in-phase χ'_M (top) and out-of-phase χ''_M (bottom) components of the *ac* susceptibility for the diluted complex **4'** under zero applied *dc* field. Inset: Arrhenius plots of relaxation times of **4'**. The black straight solid line represents the best fitting of the experimental data to the Arrhenius equation. The grey line represents the best fit to QTM plus thermally activated relaxation processes.

The relaxation times were extracted from the fitting of the frequency-dependent ac data for **1'** and **4'** to the Debye model (Figure S16). The results were then used in constructing the Arrhenius plot shown in the insets of Figure S15 and Figure 9. The fit of the high temperature data (above 6.5 K and 5.5 K for **1'** and **4'**, respectively) afforded an effective energy barrier for the reversal of the magnetization of 56.8 (4) K with $\tau_0 = 3.4 \times 10^{-8}$ s for **1'** and 54(4) K with $\tau_0 = 1.7 \times 10^{-7}$ s for **4'**. The Arrhenius plots, constructed from the temperatures and frequencies of the maxima observed for the χ''_M signals in Figure S15 and Figure 9, lead virtually to the same results, as expected. As the data deviate from linearity in the low temperature region due to the existence of the QTM relaxation process, we have fitted the temperature dependence of the relaxation time to the following equation that considers the simultaneous occurrence of both the thermal and QTM processes:

$$\tau^{-1} = \tau_{QT}^{-1} + \tau_0^{-1} \exp\left(-U_{eff}/kT\right)$$

The fit afforded the following parameters: $U_{eff} = 66(7)$ K with $\tau_0 = 1.7 \times 10^{-8}$ s and $\tau_{QT} = 0.0017(1)$ s is for **1'** and $U_{eff} = 72(3)$ K with $\tau_0 = 1.2 \times 10^{-8}$ s and $\tau_{QT} = 0.0004(2)$ s is for **4'**. The U_{eff} values are very close to that obtained for **1** and **4** under a static magnetic field of 1000 Oe when the QTM process is almost fully suppressed. The Cole-Cole plots for **1'** and **4'** (Figure S17) show in the 6-9.5 K and 5.5-8 K temperature regions semicircular shapes with α values in the range 0.44-0.33 and 0.14-0.38, respectively, thus indicating the presence of a distribution of relaxation processes in those regions. These results and the fact that compounds **2** and **5** do not

exhibit out-of-phase *ac* signals in the temperature dependence of the out-of-phase *ac* susceptibility plot, clearly point out that the relaxation processes observed in **1** and **4** arise from the M-Dy-M unit rather than from intermolecular interactions and long-range ordering. After applying a small static field of 1000 Oe, the QTM is almost suppressed due a combination of field and dilution effects (Figures S18, S19 and S20) and the fit of the relaxation times vs 1/T data for **1'** and **4'** in the 9-6 K and 9.8-7 K temperature ranges to the Arrhenius law leads (insets Figure S18 and S19), as expected, to a considerable increase of the thermal energy barrier and a decrease of τ_0 ($U_{\text{eff}} = 90(7)$ K and $\tau_0 = 1.1 \times 10^{-9}$ for **1'** and $U_{\text{eff}} = 106(4)$ K and $\tau_0 = 5.2 \times 10^{-10}$ for **4'**). As expected, the relaxation processes for **1'** and **4'** under an applied field of 1000 Oe are slower than those for **1** and **4** under the same applied field. The above results for the dilute (**1'** and **4'**) and undiluted (**1** and **4**) complexes suggest that the application of a magnetic field of 1000 Oe and the 1/10 Dy/Y dilution process slow the magnetization almost in the same extent. Therefore, it is not surprising that the combination of both effects results in an additional significant slowing of the magnetization relaxation process.

Some experimental results have shown that the substitution of a paramagnetic ion by Zn^{II} improves the SMM properties.^{[9a], [10e-h]} This is mainly due to the following facts: (i) As the M-Dy interactions are very small, the first excited state is of only a few wavenumbers above the ground state and therefore a small effective thermal energy barrier is expected. (ii) a paramagnetic ion could create a random transversal field for the Dy^{III} ions which would favour the faster QTM process and mask of the slow relaxation process^{[6a], [c], [23]} (iii) a diamagnetic ion would mitigate the intermolecular interactions that favour the fast QTM.^{[9],}

[10] .

Complexes **1** and **4** represent additional good examples of the benefit effects of such substitution as the isostructural analogues Co₂Dy and Ni₂Dy do not show maxima in the out-of-phase signal even in the presence of an applied *dc* field, [8a, b] whereas **1** and **4** show a significant thermal energy barrier of approximately 70 K. It should be noted in this context that experimental results and theoretical calculations have recently shown that all reported ZnDy complexes have higher U_{eff} than the mononuclear Dy counterparts.[10h] Therefore, it is clear the presence of ZnII helps to enhance the U_{eff} .

In order to support the presence of axial anisotropy and to provide a good description of the parameters involved in the spin relaxation processes of **1** and **4** [21,24], we have performed electronic structure calculations based on CASSCF methods. Table 2 presents the calculated energies and *g* factors for the four lowest Kramers' doublets. The excitation energies between the ground and second Kramers' doublets for **1** and **4** are 165.8 and 147.2 cm⁻¹, respectively, which fall within the typical range for DyIII CASSCF+RASSI calculations. It is worth mentioning that the experimental temperature dependence of the χ_{MT} product can be well reproduced from the energy levels obtained in the *ab initio* calculations (Figure S21) The ground states are strongly axial (*g_z* around 19.8), with almost vanishing transversal components of *g*. The easy-axis anisotropy of the DyIII ion favors the slow relaxation of the magnetization and the SMM behavior [19a, 21]. Furthermore, the calculated excitation energies in the CASSCF step are also favorable for a strongly anisotropic magnetic moment, with an almost two-fold degenerate ground state (first excitation energies 2.5 and 1.6 cm⁻¹ for complexes **1** and **4**, respectively) and a higher second excited state (139.6 and 105.6 cm⁻¹, respectively). This energy profile favors the mixing of mostly the first two CASSCF states in the ground-state wavefunction obtained with the RASSI method, both of similar shape (Figure 10 and Supporting Information Figure S22)

resulting in an oblate beta electron density for such state ^[21]. The plotted beta density of the 4f Dy^{III} electrons obtained in the CASSCF step for the ground state of the two complexes is represented in Figure 9 (Dy^{III} is 4f⁹ and the 7 alpha electrons give an isotropic spherical electron density showing the expected oblate beta electron density for such state). ^[21]

Table 2. Calculated energies (cm⁻¹), g-factors and the angle between magnetic moment with that of the ground state for the four lowest Kramers' doublets in compounds **1** and **4**.

Compound	E	g _x	g _y	g _z	angle θ
1	0.000	0.005	0.011	19.806	0.0
	165.8	1.103	1.832	15.870	14.1
	212.1	1.084	3.463	12.153	9.9
	268.8	1.389	3.748	10.325	6.0
4	0	0.010	0.017	19.825	0.0
	147.2	1.097	1.346	16.528	24.6
	189.1	2.930	4.760	11.860	162.4
	230.1	9.656	6.772	0.783	83.4

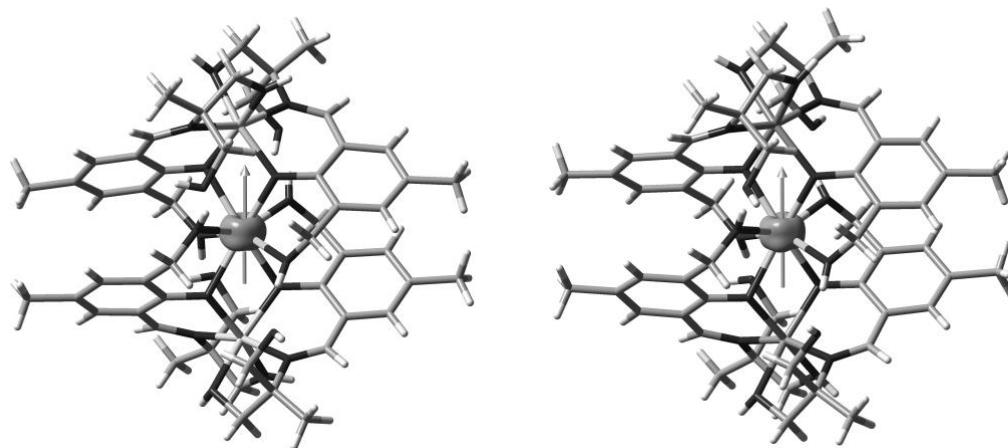


Figure 10. (above) Beta spin density of the Dy^{III} f electrons for the spin-free CASSCF ground states of **1** (left) and **4** (right), respectively. The direction of the magnetic moment of the ground state is indicated as an orange arrow.

The calculated magnetic moment of the ground state for the two complexes is aligned with the direction of the three metal atoms present in the structure. In order to verify the influence of the ligand potential on the anisotropy of the 4f electronic density of the Dy^{III} cation, we constructed electrostatic potential maps of the ligand environment projected on the Dy^{III} position by means of DFT calculations (Figure S23). The differences in the electrostatic potential are very small due to the presence of eight relatively similar oxygen atoms coordinated to the metal. There is not a clear preferential orientation to accommodate the oblate density of the Dy^{III} with the lowest electron repulsion with the ligands. Nevertheless, as indicated elsewhere, the distances with the phenoxo oxygen atoms are shorter than those with the alkoxo groups, so that the beta electron density (Figure S23) is accommodated in the equatorial region where the phenoxo groups are located. Despite the small differences in the electrostatic potential created by the oxygen atoms of the ligand, we have been able to calculate the direction of the anisotropy axis of the Dy^{III} ion by using the simple electrostatic model recently reported by Chilton *et al.*[25] As it can be

observed in Figure (Figures S24 and S25), the orientation of the anisotropic axis on each Dy³⁺ ion compare rather well with that obtained by *ab initio* methods.

To shed light on the mechanism of the magnetic relaxation in complexes **1** and **4** we computed the transversal magnetic moments between the connecting pairs of opposite magnetization (Figure 11). As can be observed, the transversal magnetic moment between the ground state Kramers' doublet is very small in both complexes (around $10^{-3} \mu_B$), which suggest that QTM is almost suppressed in the ground state. This must be the reason why **1** and **4** exhibit SMM behavior at zero field. The off diagonal terms of the transversal moments between the ground state and the excited states of opposite magnetization (related with the Orbach process) are only slightly larger than those involving the ground state (around $10^{-2} \mu_B$) and therefore the relaxation takes place through the first excited state via mainly a thermal assisted QTM process, with transversal moments between the two level of the first excited Kramers doublet of 0.55 and 0.48 μ_B for complexes **1** and **4**, respectively. Finally, the fact that the effective thermal energy barriers for **1** and **4** are almost one third of the calculated energy gap between ground and first Kramers' doublets is most likely due to the existence of QTM promoted by dipole-dipole and hyperfine interactions, which cannot be fully suppressed by dilution and/or by the applications of a small static magnetic field. It is worth mentioning that a much greater reduction of the experimental U_{eff} with regard to the calculated one (from 200 cm⁻¹ to 23 cm⁻¹) has been recently observed for a bipyramidal trigonal complex [Dy^{III}(NHPhPr₂)₃(THF)₂]_[26]. This large reduction of the U_{eff} could be due to the fact that the transversal moment between the ground state Kramers' doublet is greater than those observed in **1** and **4**, thus favouring the QTM and the reduction of the U_{eff} .

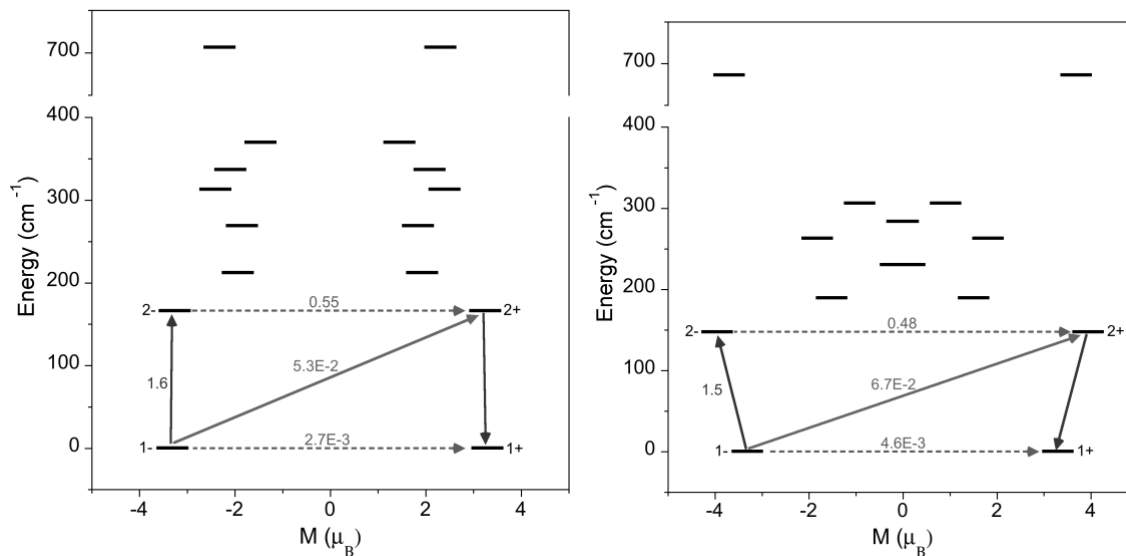


Figure 11. Calculated magnetization blocking barrier at CASSCF+RASSI level for **1** (left) and **4** (right) complexes. The black lines correspond to the Kramers' doublet as function of the magnetic moment. Dotted, solid and arrow lines correspond to quantum tunneling (and thermally-assisted quantum tunneling), Orbach and magnetization reversal mechanism, respectively. The values indicated close to the arrows indicate the matrix elements of the transition magnetic moments.

Photophysical Properties

Electronic Spectra of the Complexes (1-6)

The UV–visible absorption spectra of the free ligand (LH₄) and those of the corresponding complexes **1-6** were recorded in CH₃OH solution ($c = 1 \times 10^{-5}$ M) at 298 K and are depicted in Figure 12. The ligand-centered absorption properties of complexes **1-6** are listed in Table 3.

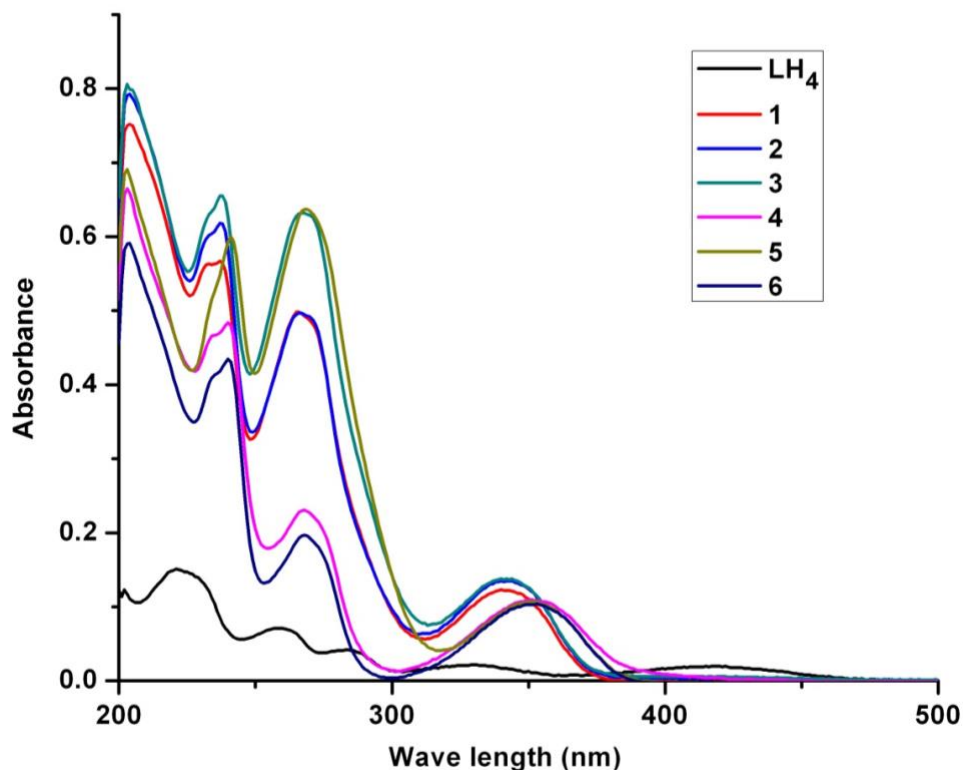


Figure 12. UV–visible absorption spectra for LH₄ and complexes **1-6** in CH₃OH solution (10⁻⁵ M).

The ligand displays absorption bands that spread up to the visible region with absorption maxima at 223, 259, 285, 328 and 415 nm. These bands originate due to ligand-centred spin-allowed singlet $\pi\text{--}\pi^*$ transition. The trends in the absorption spectra of the complexes (**1-6**) are not exactly identical to those observed for the free ligands, indicating that the singlet excited states of the ligands are perturbed by the metal coordination. They display an absorption band localized in the UV region and the absorption maxima of 223, 259 and 328 nm observed for the ligand is red-shifted in all the complexes and are found respectively at ~240, ~270 and ~345 nm which can be

attributed to the stabilization of the π^* orbitals of the ligand upon complexation with the metal ions. It is also noteworthy that the large molar absorption coefficients observed for the LH₄ implies that they have a strong ability to absorb light. The magnitudes of molar absorption coefficient values for the complexes were approximately four times higher than that of the ligand, and this trend is consistent with the presence of four ligands in each complex. In this context it is important to mention that in the metal complexes a higher extinction coefficient is observed in comparison to the ligand which indicates the possibility that the ligand can be involved in for the sensitization of lanthanide luminescence.

Table 3: Absorption properties of the ligand and complexes (**1-6**) in methanol at 298 K

Compound	Absorbance λ [nm] ($\epsilon_{\text{max}} \times 10^3 \text{ M}^{-1}\text{cm}^{-1}$) in solution
1	342 (11.94), 266 (49.60), 237(57.03)
2	340 (13.05), 265 (49.53), 238 (61.56)
3	340 (13.93), 267 (63.39), 237 (65.52)
4	352 (11.06), 268 (23), 240 (48.28)
5	351 (10.62), 269 (64), 240 (59.8)
6	350 (10.11) ,268 (19.26), 240 (43)
Ligand	413(2), 328 (2), 285 (4), 258 (7), 223 (15)

Photoluminescent properties

In order to understand the energy migration pathways for complexes **1-6**, it was necessary to determine the singlet and triplet energy levels of the ligand (LH₄). The singlet ($1\pi\pi^*$) energy level of the ligand (LH₄) was determined by reference to the wavelength of the UV-vis upper absorption edge of Gd³⁺ complexes **2** and **5** (Figure 12) and the relevant values are 363 nm (27548 cm⁻¹) and 372 nm (26881 cm⁻¹) respectively. In order to determine the triplet energy ($3\pi\pi^*$) level we have carried out the low temperature (77 K) phosphorescence measurement of the same gadolinium derivative and the values are found to be 442 nm (22,575 cm⁻¹) and 459 nm (21,778 cm⁻¹) respectively, for the complexes **2** and **5**. It is well known that Gd³⁺ complexes are ideal for determining triplet energy levels ($3\pi\pi^*$) of the ligand for the following reasons: i) the lowest-lying excited energy level ($6P_{7/2}$) for Gd³⁺ is located at 32150 cm⁻¹ which prohibits any energy transfer to the gadolinium ion from the ligand ii) the heavy paramagnetic ion effect of Gd³⁺ enhances the possibility of intersystem crossing from the singlet to the triplet state.^[27] It is therefore concluded that the luminescence observed for the gadolinium derivative is explicitly ligand-oriented.

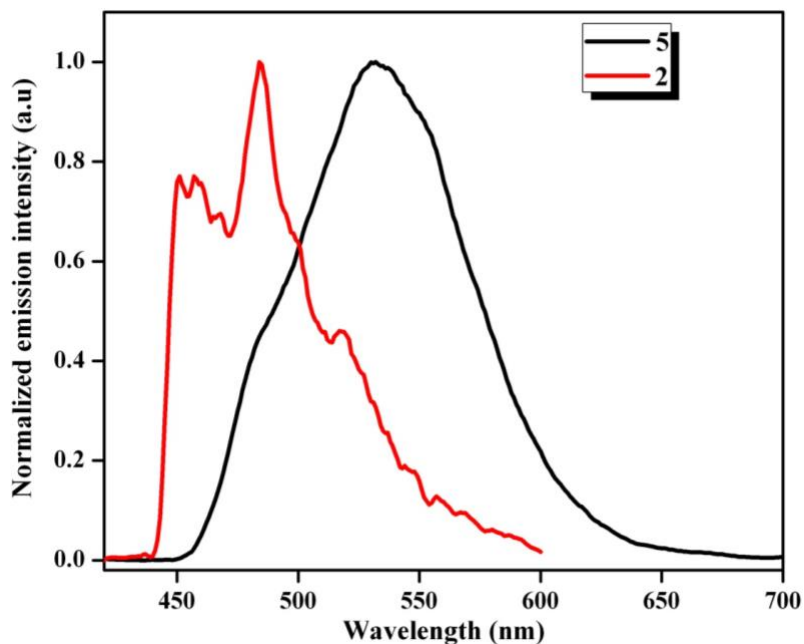


Figure 13. Phosphorescence spectra of gadolinium derivative **2** and **5** at 77 K.

It is well documented that the singlet and triplet energy gap $\{\Delta E(1\pi\pi^* - 3\pi\pi^*)\}$ of the ligand should be close to 5000 cm^{-1} for an effective inter system crossing (ISC).^[28] Thus, in the present study, it amounts to 4973 cm^{-1} for **2** and 5103 cm^{-1} for **5**, and therefore suggests that this ligand has a good capability for intersystem-crossing efficiency. The low-temperature phosphorescence spectra of the Gd^{3+} complexes **2** and **5** are shown in Figure 13.

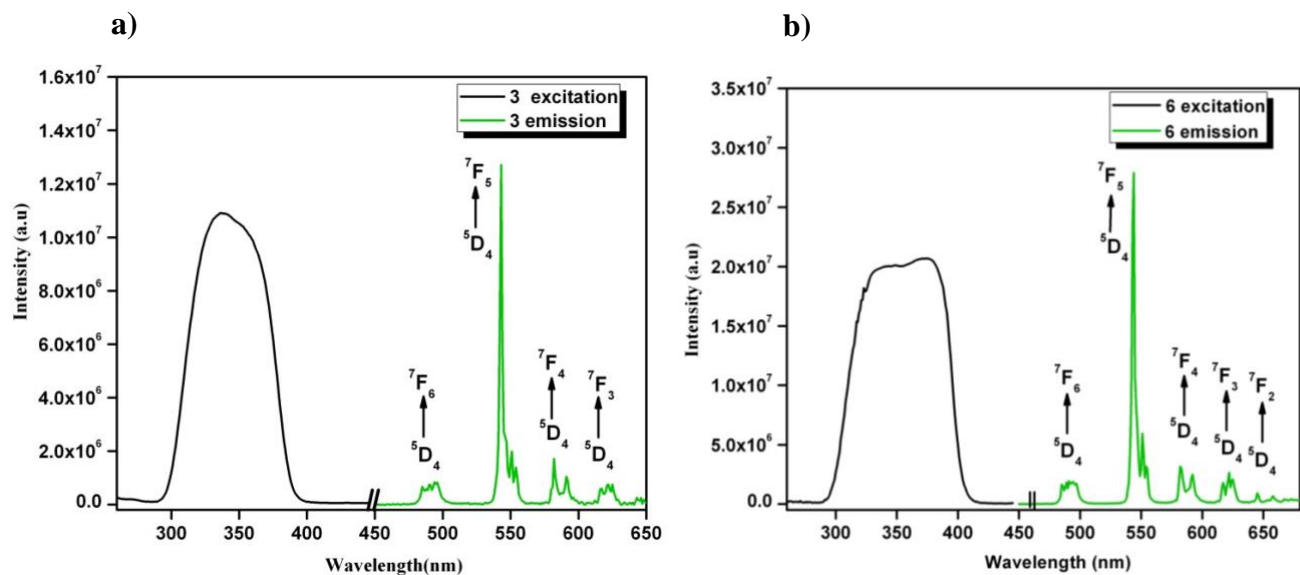


Figure 14. Room-temperature excitation and emission spectra for (a) complex **3** ($\lambda_{\text{ex}} = 340$ nm) and (b) complex **6** ($\lambda_{\text{ex}} = 375$ nm) with emission monitored at approximately 545 nm.

Among **1-6**, the only Tb(III) derivatives, **3** and **6** exhibit metal-centered luminescence (Figure S26, for Dy(III) derivative). The combined steady state excitation and emission spectra for the Tb₃₊ derivatives **3** and **6** in the solid state at room temperature are depicted in Figure 14a and 14b, respectively. The excitation spectra for **3** and **6** exhibit a broad band in the 300-400 nm region (centered at ~338 nm for **3** and ~350 nm for **6**) because of the π - π^* transitions of the ligand. Moreover, it is worth mentioning that in the cases of **3** and **6** the ligand-centered emission is not detected implying an efficient energy transfer process to metal from the ligand excited states. Upon excitation at the ligand energy level ($\lambda_{\text{ex}} = 340$ nm), **3** and **6** exhibit a series of characteristic sharp emission bands of Tb₃₊-centred at 490, 545, 585, and 620 nm, which result from deactivation of the $^5\text{D}_4$ excited state to the corresponding $^7\text{F}_j$ ground state of the Tb₃₊ ion ($J = 6$,

5, 4, 3).^[29] The more intense transition centred at 545 nm corresponds to the transition of $^5D_4 \rightarrow ^7F_5$.

Table 4: $^5D_0/^5D_4$ Lifetimes (τ_{obs}), Radiative Lifetimes (τ_{RAD}), Intrinsic Quantum Yields (Φ_{Ln}), Energy Transfer Efficiencies (Φ_{sen}), and Overall Quantum Yields (Φ_{overall}) for Complexes **3** and **6**

compound	$\tau_{\text{obs}}(\mu\text{s})$	$^a\tau_{\text{RAD}}(\mu\text{s})$	$\Phi_{\text{Ln}}(\%)$	$\Phi_{\text{sen}}(\%)$	$\Phi_{\text{overall}}(\%)$
3	606 ± 8	1474 ± 6	41	28.5	11.7 ± 1
6	799 ± 5	2337 ± 6	34	66.7	22.7 ± 2

^a τ_{RAD} = observed lifetime at 77K in CD₃OD

The room temperature excited state 5D_4 (Tb_{3+}) luminescence life time values were measured (monitored at 545 nm) and were found to be $\tau_0 = 0.606$ ms for compound **3** and 0.799 ms for compound **6**. Actually in both the instances a single exponential decay curve was found highlighting the presence of a single terbium emitting center. Even though there exists a less favourable Franck Condon overlap factor with the fourth vibrational overtone of the proximate OH oscillators ($\nu_{\text{OH}} \sim 3300$ to 3500 cm^{-1}) to that of the Tb_{3+} emitting centre, the 5D_4 lifetime values of Tb_{3+} complexes **3** and **6** are found to be essentially temperature dependent, with τ_{RAD} varying by more than twice (Table 4) while going from 298 (Figure 15) to 77 K (Figure S27), thereby indicating the dominant contribution of a temperature-dependent vibrational quenching which is usually observed in the case of luminescent heterometallic transition metal-lanthanide based complexes^[16h] Most probably, the non-radiative deactivation of the terbium emitting state in the $[\text{Zn}^{\text{II}}\text{Tb}^{\text{III}}]$ or $[\text{Mg}^{\text{II}}\text{Tb}^{\text{III}}]$ complex is dominated by an efficient back-energy transfer process from the 5D_4 level of terbium to the triplet states of the ligand. For **3**, the energy of the ligand

triplet state (ca. 22,575 cm⁻¹) lies ca. 2075 cm⁻¹ above the ⁵D₄ level of terbium (20,500 cm⁻¹), while the same for complex **6** is found to be 1278 cm⁻¹. Hence the low energy difference between the ligand triplet and metal centered emissive excited states in complex **6** will trigger the rate of thermally activated back energy transfer and is evidenced from the nearly thrice enhanced decay profile at 77K for complex **6** (Table 4).

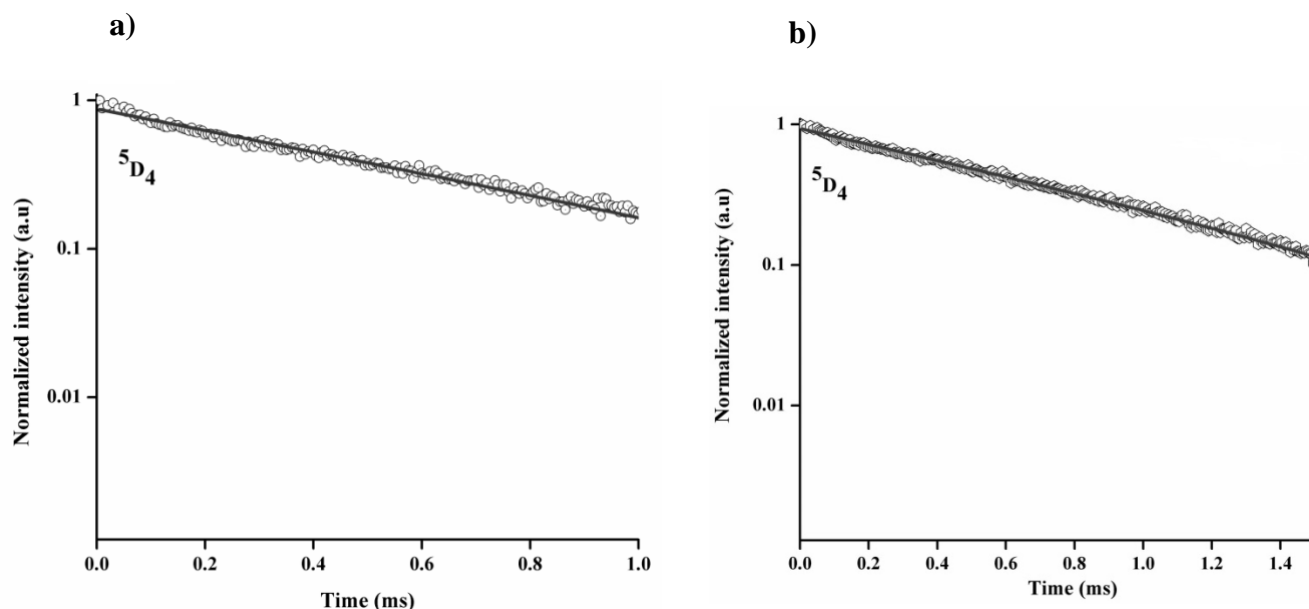


Figure 15. Phosphorescence decay of (a) complex **3** and (b) complex **6**. The emission was monitored at 545 nm (⁵D₄ → ⁷F₅) respectively in solid state at 298 K.

To quantify the ability of the ligands designed to sensitize the luminescence of lanthanides, and to draw conclusions concerning the relationship between the structure and the properties, it was appropriate to analyze the emission in terms of eq 1 (below) where Φ_{overall} and Φ_{Ln} , represent the ligand-sensitized and intrinsic luminescence quantum yields of Ln³⁺; Φ_{sen} represents the

efficiency of the ligand-to-metal energy transfer and $\tau_{\text{obs}}/\tau_{\text{RAD}}$ are the observed and the radiative lifetimes of Ln^{3+} .^[30]

$$\Phi_{\text{Overall}} = \Phi_{\text{sen}} \times \Phi_{\text{Ln}} = \Phi_{\text{sen}} \times (\tau_{\text{obs}}/\tau_{\text{RAD}}) \quad (1)$$

The intrinsic quantum yield for Tb^{3+} (Φ_{Tb}) was estimated using eq 2 with the assumption that the decay process at 77 K in a deuterated solvent is purely radiative.^[31]

$$\Phi_{\text{Tb}} = \tau_{\text{obs}}(298 \text{ K})/\tau_{\text{obs}}(77 \text{ K}) \quad (2)$$

Table 4 summarizes the Φ_{Overall} , Φ_{Ln} , and Φ_{sen} . In the case of terbium luminescence, solid-state measurements gave an absolute quantum yield of 11.7 % for complex **3** compared with 22.7 % for complex **6**. The closeness of the ligand triplet energy towards terbium emitting centre in complex **6** provide efficient energy transfer as evidenced from the impressive sensitization efficiency of 66.7 % which in turn give rise to a 22.7 % quantum yield when compared to complex **3**, where the sensitization efficiency and quantum yields are found to be 28% and 11.7%, respectively.

Conclusion

The efficacy of the ligand LH_4 in synthesizing trinuclear heterometallic complexes allowed us to synthesize a new series of isostructural complexes containing $[\text{Mg}_2\text{Ln}]^{3+}$ [$\text{Ln} = \text{Dy}$ (**1**), Gd (**2**) and Tb (**3**)] and $[\text{Zn}_2\text{Ln}]^{3+}$ [$\text{Ln} = \text{Dy}$ (**4**), Gd (**5**) and Tb (**6**)] cores. Unlike the previous cases [8a, 8b], we have deliberately incorporated diamagnetic metal ions *viz.* Zn^{2+} and Mg^{2+} within the cluster hoping to enhance the SMM properties by suppressing quantum tunnelling as well as increasing the energy gap between ground state and excited state. Complexes **1** and **4** show SMM behavior with the following parameters: $U_{\text{eff}} = 72(2) \text{ K}$ with $\tau_0 = 8 \times 10^{-9} \text{ s}$ for the SR

process and $U_{\text{eff}} = 61(2)$ K with $\tau_0 = 4 \times 10^{-7}$ s for the FR process in complex **1**, and $U_{\text{eff}} = 67(3)$ K with $\tau_0 = 4.5 \times 10^{-8}$ s in complex **4**. *Ac* susceptibility measurements on the magnetic diluted samples of **1** and **4**, named as **1'** and **4'**, which were prepared through crystallization with the diamagnetic and isostructural Mg_2Y and Zn_2Y complexes using a Dy/Y molar ratio of 1:10, clearly show that the relaxation dynamics is not due to intermolecular interactions and/or long range ordering and therefore has single molecular origin. Interestingly, the diluted compounds **1'** and **4'** exhibits SMM behavior under zero magnetic field and QTM at low temperature. The fit to a combination of activated and QTM relaxation processes afforded the following parameters: $U_{\text{eff}} = 66(7)$ K with $\tau_0 = 1.7 \times 10^{-8}$ s and $\tau_{\text{QTM}} = 0.0017(1)$ s. $U_{\text{eff}} = 72(3)$ K with $\tau_0 = 1.2 \times 10^{-8}$ s and $\tau_{\text{QTM}} = 0.0004(2)$ s. The U_{eff} values are very close to that obtained for **1** and **4** under a static magnetic field of 1000 Oe. After applying a small static field of 1000 Oe on **1'** and **4'**, the QTM is almost suppressed due a combination of field and dilution effects and, as expected, the thermal energy barrier undergoes an slight increase with the concomitant decrease of τ_0 ($U_{\text{eff}} = 90(7)$ K and $\tau_0 = 1.1 \times 10^{-9}$ for **1'** and $U_{\text{eff}} = 106(4)$ K and $\tau_0 = 5.2 \times 10^{-10}$ for **4'**). The results for the diluted complexes clearly indicate that the relaxation of magnetization originates from the M-Dy-M unit rather than from intermolecular interactions and/or long-range ordering. Ab initio calculations, carried out on complexes **1** and **4**, confirm that the magnetic anisotropy is uniaxial along the M-Dy-M unit and that the relaxation takes place through the first excited state via mainly a thermal assisted QTM process. Additionally, the effectiveness of the ligand $[\text{LH}_3]_2^-$ to act as "*antenna*" has discussed in details here. Both the Tb^{III} based complexes display bright green luminescence efficiency in the solid state with sensitization efficiency of 66.7 % for **6** but for **3** the sensitization efficiency is 28% due to poor matching of the triplet state of the ligand

with the emissive excited states of the metal ion. Thus, compound **6** may render as pledging candidate for use in various photonic applications.

Experimental Section

Reagents and General Procedures. Solvents and other general reagents used in this work were purified according to standard procedures.^[32] $\text{Mg}(\text{NO}_3)_2 \cdot 6\text{H}_2\text{O}$ and 2-amino-2-methylpropane-1,3-diol was obtained from S.D. Fine Chemicals, Mumbai, India. 2,6-Bis(hydroxymethyl)-4-methylphenol, $\text{Dy}(\text{NO}_3)_3 \cdot 5\text{H}_2\text{O}$, $\text{Tb}(\text{NO}_3)_3 \cdot 5\text{H}_2\text{O}$, $\text{Gd}(\text{NO}_3)_3 \cdot 6\text{H}_2\text{O}$, $\text{Y}(\text{NO}_3)_3 \cdot 6\text{H}_2\text{O}$ and MnO_2 were obtained from Sigma Aldrich Chemical Co. and were used as received. 2-(2-Hydroxy-3-(hydroxymethyl)-5-methylbenzylideneamino)-2-methylpropane-1,3-diol (LH_4) was synthesized by a procedure as reported earlier.^[8b]

Instrumentation. Melting points were measured using a JSGW melting point apparatus and are uncorrected. IR spectra were recorded as KBr pellets on a Bruker Vector 22 FT IR spectrophotometer operating at 400-4000 cm^{-1} . Elemental analyses of the compounds were obtained from Thermoquest CE instruments CHNS-O, EA/110 model. Electrospray ionization mass spectrometry (ESI-MS) spectra were recorded on a Micromass Quattro II triple quadrupole mass spectrometer.

Magnetic Properties: The variable temperature (2-300 K) magnetic susceptibility measurements on a polycrystalline sample of **1** and **4** under an applied field of 1000 Oe were carried out with a Quantum Design SQUID MPMS XL-5 device. Ac susceptibility measurements under different applied static fields were performed using an oscillating *ac* field of 3.5 Oe and *ac* frequencies ranging from 10 to 1000 Hz. The experimental susceptibilities were corrected for the sample holder and diamagnetism of the constituent atoms by using Pascal's

tables. A pellet of the sample cut into very small pieces was placed in the sample holder to prevent any torquing of the microcrystals.

Photophysical Characterization. The absorbance spectrum of the ligand and complexes were measured on a Shimadzu, UV-2450 UV-vis-NIR spectrophotometer. The photoluminescence (PL) spectrum of the complexes were recorded on a Spex-Fluorolog FL22 spectrofluorimeter equipped with a double grating 0.22 m Spex 1680 monochromator and a 450 W Xe lamp as the excitation source and a Hamamatsu R928P photomultiplier tube detector. Emission and excitation spectra were corrected for source intensity (lamp and grating) by standard correction curves. The lifetime measurements were carried out at room temperature using a Spex 1040D phosphorimeter. Photoluminescence quantum yield of the powder sample as well as in the solution state were measured using a calibrated integrating sphere in a SPEX Fluorolog Spectrofluorimeter. A Xe-arc lamp was used to excite the sample placed in the sphere, with 365 nm as the excitation wavelength. Absolute quantum yield was calculated on the basis of the de Mello method^[33] using the equation

$$\Phi_{\text{PL}} = [E_i(\lambda) - (1 - A)E_o(\lambda)] / L_e(\lambda)A \quad (1)$$

In eq 2

$$A = [L_o(\lambda) - L_i(\lambda)] / L_o(\lambda) \quad (2)$$

Where $E_i(\lambda)$ and $E_o(\lambda)$ are respectively the integrated luminescence as a result of direct excitation of sample and secondary excitation. A is the absorbance of the sample calculated using eq 1. $L_i(\lambda)$ is the integrated excitation when the sample is directly excited, $L_o(\lambda)$ is the integrated

excitation when the excitation light first hits the sphere and reflects to the sample, and $L_e(\lambda)$ is the integrated excitation profile for an empty sphere.

X-ray Crystallography. The crystal data for the compounds have been collected on a Bruker SMART CCD diffractometer (MoK α radiation, $\lambda = 0.71073$ Å). The program SMART_[34a] was used for collecting frames of data, indexing reflections, and determining lattice parameters, SAINT_[34a] for integration of the intensity of reflections and scaling, SADABS_[34b] for absorption correction, and SHELXTL_[29c,d] for space group and structure determination and least-squares refinements on F₂. All the structures were solved by direct methods using the program SHELXS-97_[34e] and refined by full-matrix least-squares methods against F₂ with SHELXL-97._[34e] Hydrogen atoms were fixed at calculated positions and their positions were refined by a riding model. All non-hydrogen atoms were refined with anisotropic displacement parameters. The crystallographic figures have been generated using Diamond 3.1e software._[34f] The crystal data and the cell parameters for compounds **1-6** are summarized in Table 5 and Table 6. The crystal data and the cell parameters for **1'** and **4'** are summarized in Table S9. CCDC- 1020216 (for **1**), CCDC-1020217 (for **2**), CCDC-1020218 (for **3**), CCDC-1020219 (for **4**), CCDC-1020220 (for **5**), CCDC-1020221 (for **6**), CCDC-1040620 (for **1'**) and CCDC-1040621 (for **4'**) contain the crystallographic data for the complexes reported in this paper. This data can be obtained free of charge from the Cambridge Crystallographic Data Centre via www.ccdc.cam.ac.uk/data_request/cif.

Table 5: Crystal data and structure refinement parameters for **1-3**.

	1	2	3
Formula	C ₅₄ H ₈₀ DyMg ₂ N ₇ O ₂₈	C ₁₀₈ H ₁₆₀ Gd ₂ Mg ₄ N ₁₄ O ₅₅	C ₁₀₈ H ₁₆₄ Mg ₄ N ₁₄ O ₅₇ Tb ₂
M/g	1486.37	2946.24	2985.61

Crystal system	Monoclinic	Monoclinic	Monoclinic
Space group	$P2_1/n$	$P2_1/n$	$P2_1/n$
$a/\text{\AA}$	14.912(5)	14.965(7)	14.913(5)
$b/\text{\AA}$	22.627(5)	22.945(11)	22.633(5)
$c/\text{\AA}$	20.411(5)	20.737(10)	20.453(5)
β (°)	92.978(5)	93.529(9)	93.100(5)
$V/\text{\AA}^3$	6878(3)	7107(6)	6893(3)
Z	4	2	2
$\rho/\text{g cm}^{-3}$	1.435	1.376	1.438
μ/mm^{-1}	1.189	1.032	1.130
$F(000)$	3068	3040	3088
Cryst size (mm ³)	0.055x0.042x 0.031	0.059x0.045x 0.025	0.068x0.042x 0.021
θ range (deg)	4.10 to 25.03	4.15 to 25.02	4.09 to 25.02
Limiting indices	-15 $\leq h \leq$ 17 -26 $\leq k \leq$ 24 -24 $\leq l \leq$ 19	-17 $\leq h \leq$ 17 -25 $\leq k \leq$ 27 -24 $\leq l \leq$ 24	-13 $\leq h \leq$ 17 -26 $\leq k \leq$ 26 -24 $\leq l \leq$ 24
Reflns collected	35644	51654	35761
Indreflns	12082 [$R(\text{int}) = 0.0541$]	12470 [$R(\text{int}) = 0.0475$]	12082 [$R(\text{int}) = 0.0690$]
Completeness to θ (%)	99.4 %	99.3 %	99.2 %
Refinement method	Full-matrix-block least-squares on F_2	Full-matrix-block least-squares on F_2	Full-matrix-block least-squares on F^2
Data/restraints/ parameters	12082 / 24 / 869	12470 / 66 / 866	12082 / 59 / 878
Goodness-of-fit on F_2	1.055	1.161	1.030
Final R indices [$I > 2\theta(I)$]	$R_1 = 0.0796$ $wR_2 = 0.2272$	$R_1 = 0.0763$ $wR_2 = 0.2085$	$R_1 = 0.0920$ $wR_2 = 0.2487$
R indices (all data)	$R_1 = 0.1097$ $wR_2 = 0.2517$	$R_1 = 0.0903$ $wR_2 = 0.2179$	$R_1 = 0.1322$ $wR_2 = 0.2784$
Largest diff. peak and hole($\text{e} \cdot \text{\AA}^{-3}$)	1.761 and -0.775	2.056 and -1.473	2.226 and -0.770

Table 6: Crystal data and structure refinement parameters for **4-6**.

	4	5	6
Formula	C ₁₀₈ H ₁₆₄ Dy ₂ N ₁₄ O ₅₇ Zn ₄	C ₅₅ H ₈₄ GdN ₇ O ₂₈ Zn ₂	C ₁₀₈ H ₁₆₀ N ₁₄ O ₅₅ Tb ₂ Zn ₄
M/g	3157.10	1579.28	3113.82
Crystal system	Monoclinic	Monoclinic	Monoclinic
Space group	<i>P</i> 2 ₁ / <i>n</i>	<i>P</i> 2 ₁ / <i>n</i>	<i>P</i> 2 ₁ / <i>n</i>
<i>a</i> /Å	15.029(5)	15.030(5)	15.068(5)
<i>b</i> /Å	22.431(5)	22.444(5)	22.488(5)
<i>c</i> /Å	20.077(5)	20.107(5)	20.177(5)
β (°)	92.961(5)	92.928(5)	93.039(5)
<i>V</i> /Å ³	6759(3)	6774(3)	6827(3)
<i>Z</i>	2	4	2
ρ /g cm ⁻³	1.551	1.549	1.438
μ /mm ⁻¹	1.885	1.757	1.515
<i>F</i> (000)	3236	3244	3192
Cryst size (mm ³)	0.066 x 0.047 x 0.023	0.057 x 0.031 x 0.012	0.051 x 0.032 x 0.023
θ range (deg)	4.08 to 25.03	4.08 to 25.03	4.13 to 25.03
Limiting indices	-17 \leq h \leq 17 -26 \leq k \leq 26 -23 \leq l \leq 23	-17 \leq h \leq 17 -26 \leq k \leq 26 -23 \leq l \leq 23	-17 \leq h \leq 10 -26 \leq k \leq 26 -24 \leq l \leq 23
Reflns collected	38515	38018	35090
Indreflns	11881 [<i>R</i> (int) = 0.0459]	11909 [<i>R</i> (int) = 0.0617]	11991 [<i>R</i> (int) = 0.0752]
Completeness to θ (%)	99.5	99.5	99.5
Refinement method	Full-matrix-block least-squares on <i>F</i> ₂	Full-matrix-block least-squares on <i>F</i> ₂	Full-matrix-block least- squares on <i>F</i> ²
Data/restraints/ parameters	11881 / 21 / 875	11909 / 21 / 875	11991 / 22 / 866
Goodness-of-fit on <i>F</i> ₂	1.126	1.084	1.024
Final <i>R</i> indices [<i>I</i> > 2 θ (<i>I</i>)]	<i>R</i> ₁ = 0.0900 <i>wR</i> ₂ = 0.2041	<i>R</i> ₁ = 0.0880 <i>wR</i> ₂ = 0.2105	<i>R</i> ₁ = 0.0873 <i>wR</i> ₂ = 0.2256
<i>R</i> indices (all data)	<i>R</i> ₁ = 0.1162 <i>wR</i> ₂ = 0.2172	<i>R</i> ₁ = 0.1304 <i>wR</i> ₂ = 0.2297	<i>R</i> ₁ = 0.1357 <i>wR</i> ₂ = 0.2570
Largest diff. peak and hole(e · Å ⁻³)	1.851 and -1.836	2.144 and -1.582	1.828 and -1.416

Computational Details

Low energy spectra and g factors of the four lowest Kramer's doublets of the two studied complexes were obtained by means of CASSCF+RASSI calculations, as implemented in the MOLCAS 7.8 software package.^[24] The approach is divided in two steps: (i) CASSCF(7,9) calculations for three different multiplicities (sextet, quartet and doublet) (ii) The effect of spin-orbit coupling on the basis of the converged wave functions obtained in the previous step is included by the Restricted Active Space State Interaction (RASSI) method. Spin Hamiltonian parameters (such as g factors) can be calculated from the wave functions resulting after the state interaction step employing the SINGLE_ANISO program. We included 21, 128 and 98 states for the sextet, quartet and doublet CASSCF calculations, while the employed basis set has the following contractions: Dy [9s8p6d4f3g2h]; Zn [4s3p2d1f]; O [4s3p2d1f]; N [4s3p2d1f]; C [3s2p]; H [2s]. The structure of the model was extracted from the corresponding X-ray structure without any ligand simplification. Electrostatic potential maps were obtained by B3LYP calculations as implemented in the Gaussian09^[35] using a TZVP basis set and the geometry for the ligand environment of the previous CASSCF+RASSI calculations and removing the central Dy^{III} ion.

Synthesis

General Procedure for the Synthesis of 1-6

A general procedure was applied for the preparation of **1-6**. To a solution of LH₄ in methanol (30 mL), Ln(NO₃)₃· n H₂O (For **1**, $n = 5$; **2**, $n = 6$; **3**, $n = 5$; **4**, $n = 5$; **5**, $n = 6$; **6**, $n = 5$;) was added. Then, triethylamine was added to the above solution and stirred it for 15 minutes. After that a methanolic solution of Mg(NO₃)₂·6H₂O or Zn(NO₃)₂·6H₂O was added drop wise, resulting in a yellow solution. The reaction mixture was stirred for a further period of 12 h to afford a clear

solution. This was filtered and the filtrate evaporated to dryness. The residue obtained was washed with diethyl ether, dried, dissolved in methanol/chloroform (1:1) and kept for crystallization under vapour diffusion conditions. After 4-7 days, pure crystalline products suitable for X-ray diffraction were isolated. Specific details of each reaction and the characterization data of the products obtained are given below.

[Mg₂Dy(LH₃)₄]·3NO₃·2MeOH·1H₂O (1)

Quantities: Mg(NO₃)₂·6H₂O (0.036 g, 0.14 mmol), Dy(NO₃)₃·5H₂O (0.03 g, 0.07 mmol), LH₄ (0.08 g, 0.29 mmol) and Et₃N (0.06 ml, 0.59 mmol). Yield: 0.072 g, 69% (based on Dy). Mp: >260°C. IR (KBr) cm⁻¹: 3208 (b), 2929 (w), 2881 (w), 1637 (s), 1569 (s), 1456 (s), 1384 (s), 1294 (s), 1269 (s), 1172 (w), 1038 (s), 999 (w), 973 (w), 819 (s). ESI-MS *m/z*, ion: 406.79, [C₅₂H₇₂N₄O₁₆Mg₂Dy]₃⁺. Anal. Calcd. for C₅₄H₈₂DyMg₂N₇O₂₈ (1488.42): C, 43.58; H, 5.55; N, 6.59. Found: C, 43.68; H, 5.29; N, 6.89.

[Mg₂Gd(LH₃)₄]·3NO₃·2MeOH·0.5H₂O (2)

Quantities: Mg(NO₃)₂·6H₂O (0.036 g, 0.14 mmol), Gd(NO₃)₃·6H₂O (0.03 g, 0.07 mmol), LH₄ (0.08 g, 0.29 mmol) and Et₃N (0.06 ml, 0.59 mmol). Yield: 0.066 g, 64% (based on Gd). Mp: >260°C. IR (KBr) cm⁻¹: 3207 (b), 2927 (w), 2880 (w), 1638 (s), 1568 (s), 1456 (s), 1384 (s), 1295 (s), 1270 (s), 1173 (w), 1036 (s), 998 (w), 976 (w), 819 (s). ESI-MS *m/z*, ion: 404.78, [C₅₂H₇₂N₄O₁₆Mg₂Gd]₃⁺. Anal. Calcd. for C₅₄H₈₁N₇O_{27.5}Mg₂Gd (1473.40): C, 44.00; H, 5.54; N, 6.65. Found: C, 44.21; H, 5.42; N, 6.83.

[Mg₂Tb(LH₃)₄]·3NO₃·2MeOH·1.5H₂O (3)

Quantities: Mg(NO₃)₂·6H₂O (0.036 g, 0.14 mmol), Tb(NO₃)₃·5H₂O (0.03 g, 0.07 mmol), LH₄ (0.08 g, 0.29 mmol) and Et₃N (0.06 ml, 0.59 mmol). Yield: 0.069 g, 66% (based on Tb). Mp:

>260°C. IR (KBr) cm^{-1} : 3208 (b), 2927 (w), 2883 (w), 1638 (s), 1568 (s), 1456 (s), 1385 (s), 1299 (s), 1271 (s), 1169 (w), 1037 (s), 999 (w), 973 (w), 819 (s). ESI-MS m/z , ion: 405.11, $[\text{C}_{52}\text{H}_{72}\text{N}_4\text{O}_{16}\text{Mg}_2\text{Tb}]^{3+}$. Anal. Calcd. for $\text{C}_{54}\text{H}_{83}\text{N}_7\text{O}_{28.5}\text{Mg}_2\text{Tb}$ (1492.42): C, 43.42; H, 5.60; N, 6.56. Found: C, 43.31; H, 5.59; N, 6.62.

$[\text{Zn}_2\text{Dy}(\text{LH}_3)_4] \cdot 3\text{NO}_3 \cdot 2\text{MeOH} \cdot 1.5\text{H}_2\text{O}$ (4)

Quantities: $\text{Zn}(\text{NO}_3)_2 \cdot 6\text{H}_2\text{O}$ (0.042 g, 0.14 mmol), $\text{Dy}(\text{NO}_3)_3 \cdot 5\text{H}_2\text{O}$ (0.03 g, 0.07 mmol), LH_4 (0.08 g, 0.29 mmol) and Et_3N (0.06 ml, 0.59 mmol). Yield: 0.075 g, 67.82 % (based on Dy). Mp: >260°C. IR (KBr) cm^{-1} : 3225 (b), 2924 (w), 2882 (w), 1635 (s), 1567 (s), 1455 (s), 1384 (s), 1293 (s), 1223 (s), 1170 (w), 1048 (s), 998 (w), 974 (w), 819 (w), 794 (w). ESI-MS m/z , ion: 435.09, $[\text{C}_{52}\text{H}_{72}\text{N}_4\text{O}_{16}\text{Zn}_2\text{Dy}]^{3+}$. Anal. Calcd. for $\text{C}_{54}\text{H}_{83}\text{DyN}_7\text{O}_{28.5}\text{Zn}_2$ (1579.58): C, 41.06; H, 5.30; N, 6.21. Found: C, 41.15; H, 5.25; N, 6.35.

$[\text{Zn}_2\text{Gd}(\text{LH}_3)_4] \cdot 3\text{NO}_3 \cdot 3\text{MeOH}$ (5)

Quantities: $\text{Zn}(\text{NO}_3)_2 \cdot 6\text{H}_2\text{O}$ (0.042 g, 0.14 mmol), $\text{Gd}(\text{NO}_3)_3 \cdot 6\text{H}_2\text{O}$ (0.03 g, 0.07 mmol), LH_4 (0.08 g, 0.29 mmol) and Et_3N (0.06 ml, 0.59 mmol). Yield: 0.078 g, 70.55 % (based on Gd). Mp: >260°C. IR (KBr) cm^{-1} : 3226 (b), 2925 (w), 2880 (w), 1635 (s), 1567 (s), 1455 (s), 1383 (s), 1295 (s), 1220 (s), 1173 (w), 1047 (s), 999 (w), 974 (w), 819 (w), 795 (w). ESI-MS m/z , ion: 433.09, $[\text{C}_{52}\text{H}_{72}\text{N}_4\text{O}_{16}\text{Zn}_2\text{Gd}]^{3+}$. Anal. Calcd. for $\text{C}_{55}\text{H}_{84}\text{GdN}_7\text{O}_{28}\text{Zn}_2$ (1579.28): C, 41.83; H, 5.36; N, 6.21. Found: C, 41.90; H, 5.51; N, 6.32.

$[\text{Zn}_2\text{Tb}(\text{LH}_3)_4] \cdot 3\text{NO}_3 \cdot 2\text{MeOH} \cdot 0.5\text{H}_2\text{O}$ (6)

Quantities: $\text{Zn}(\text{NO}_3)_2 \cdot 6\text{H}_2\text{O}$ (0.042 g, 0.14 mmol), $\text{Tb}(\text{NO}_3)_3 \cdot 5\text{H}_2\text{O}$ (0.03 g, 0.07 mmol), LH_4 (0.08 g, 0.29 mmol) and Et_3N (0.06 ml, 0.59 mmol). Yield: 0.071 g, 65.10 % (based on Tb). Mp: >260°C. IR (KBr) cm^{-1} : 3220 (b), 2922 (w), 2881 (w), 1635 (s), 1568 (s), 1456 (s), 1383 (s), 1291 (s), 1221 (s), 1169 (w), 1045 (s), 998 (w), 971 (w), 819 (w), 796 (w). ESI-MS m/z , ion:

434.09, $[\text{C}_{52}\text{H}_{72}\text{N}_4\text{O}_{16}\text{Zn}_2\text{Tb}]_{3+}$. Anal. Calcd. for $\text{C}_{54}\text{H}_{81}\text{N}_7\text{O}_{27.5}\text{TbZn}_2$ (1557.99): C, 41.63; H, 5.24; N, 6.29. Found: C, 41.71; H, 5.15; N, 6.45.

Procedure for the Synthesis of 1' and 4'

This diluted complexes were prepared by following the same method as that for **1-6** but here we have used 0.007 mmol of $\text{Dy}(\text{NO}_3)_3 \cdot 5\text{H}_2\text{O}$ and 0.063 mmol of $\text{Y}(\text{NO}_3)_3 \cdot 6\text{H}_2\text{O}$ instead of 0.07 mmol of $\text{Dy}(\text{NO}_3)_3 \cdot 5\text{H}_2\text{O}$. As a crystallization solvent here we have used Methanol/Acetonitrile mixture. Specific details of each reaction and the characterization data of the products obtained are given below.

$[\text{Mg}_2\text{Dy}_{0.14}\text{Y}_{0.86}(\text{LH}_3)_4] \cdot 3\text{NO}_3 \cdot 2\text{MeOH} \cdot \text{CH}_3\text{CN}$ (1')

Quantities: $\text{Mg}(\text{NO}_3)_2 \cdot 6\text{H}_2\text{O}$ (0.036 g, 0.14 mmol), $\text{Dy}(\text{NO}_3)_3 \cdot 5\text{H}_2\text{O}$ (0.003 g, 0.007 mmol), $\text{Y}(\text{NO}_3)_3 \cdot 6\text{H}_2\text{O}$ (0.0241g, 0.063 mmol), LH_4 (0.08 g, 0.29 mmol) and Et_3N (0.06 ml, 0.59 mmol). Yield: 0.076 g, 75% (based on Mg). Mp: $>260^\circ\text{C}$. IR (KBr) cm^{-1} : 3210 (b), 2931 (w), 2880 (w), 1635 (s), 1566 (s), 1455 (s), 1384 (s), 1298 (s), 1271 (s), 1173 (w), 1035 (s), 998 (w), 974 (w), 819 (s). Anal. Calcd. for $\text{C}_{56}\text{H}_{83}\text{Dy}_{0.14}\text{Mg}_2\text{N}_8\text{O}_{27}\text{Y}_{0.86}$ (1448.08): C, 46.44; H, 5.77; N, 7.73. Found: C, 46.63; H, 5.84; N, 7.79.

$[\text{Zn}_2\text{Dy}_{0.1}\text{Y}_{0.9}(\text{LH}_3)_4] \cdot 3\text{NO}_3 \cdot 2\text{MeOH} \cdot 2\text{H}_2\text{O} \cdot \text{CH}_3\text{CN}$ (4')

Quantities: $\text{Zn}(\text{NO}_3)_2 \cdot 6\text{H}_2\text{O}$ (0.042 g, 0.14 mmol), $\text{Dy}(\text{NO}_3)_3 \cdot 5\text{H}_2\text{O}$ (0.003 g, 0.007 mmol), $\text{Y}(\text{NO}_3)_3 \cdot 6\text{H}_2\text{O}$ (0.0241g, 0.063 mmol), LH_4 (0.08 g, 0.29 mmol) and Et_3N (0.06 ml, 0.59 mmol). Yield: 0.071 g, 64.88 % (based on Zn). Mp: $>260^\circ\text{C}$. IR (KBr) cm^{-1} : 3222 (b), 2926 (w), 2879 (w), 1632 (s), 1568 (s), 1451 (s), 1386 (s), 1289 (s), 1224 (s), 1173 (w), 1049 (s), 999 (w), 974 (w), 819 (w), 795 (w). Anal. Calcd. for $\text{C}_{56}\text{H}_{87}\text{Dy}_{0.10}\text{N}_8\text{O}_{29}\text{Y}_{0.90}\text{Zn}_2$ (1563.29): C, 43.02; H, 5.60; N, 7.16. Found: C, 43.12; H, 5.66; N, 7.25.

Acknowledgments

We are thankful to the Department of Science and Technology, New Delhi, for financial support. SD, AD and SB thanks CSIR, India for Senior Research Fellowship. VC is thankful to the Department of Science and Technology for a J. C. Bose National Fellowship. EC and ER are thankful for financial support from the Spanish *Ministerio de Economía y Competitividad* (Project CTQ-2011-24478 and CTQ2011-23862-C02-01). EC is also thankful to the *Junta de Andalucía* (FQM-195, the Project of excellence P11-FQM-7756) and the University of Granada. S. T-P is thankful to Junta de Andalucía for a postdoctoral contract. E.R. also thanks Generalitat de Catalunya for an ICREA Academia fellowship. The authors thankfully acknowledge the computer resources, technical expertise and assistance provided by the CESCA.

Supporting Information Available: ESI-MS, DIAMOND pictures of **2–6**, Tables of list of bond parameters of **2–6**, Table for Shape Measurement calculation and Structural parameters for characterizing the square-antiprism geometry, X-ray powder diffractograms for compound **4** and the diluted complexes **4'** and **1'**, and some magnetic plots for **1**, **4** and their respective diluted samples, Beta spin density of the Dy^{III} f electrons for the first three excited states (first excited state) using the spin-free CASSCF of **4** and **1**, DFT calculated (B3LYP/ TZV), CASSCF *ab initio* calculations for the direction of local anisotropy axis, Room-temperature excitation and emission spectra for **4** and **1**, phosphorescence decay of **3** and **6** in solid state at 77 K.

References

- [1] a) L. Bogani, W. Wernsdorfer, *Nat. Mater.* **2008**, 7, 179-186; b) M. Mannini, F. Pineider, C. Danieli, F. Totti, L. Sorace, P. Sainctavit, M. A. Arrio, E. Otero, L. Joly, J. C. Cezar, A. Cornia,

R. Sessoli, *Nature* **2010**, 468, 417-421; c) M. Urdampilleta, N. V. Nguyen, J. P. Cleuziou, S. Klyatskaya, M. Ruben, W. Wernsdorfer, *Int. J. Mol. Sci.* **2011**, 12, 6656-6667.

[2] a) M. Affronte, *J. Mater. Chem.* **2009**, 19, 1731-1737; b) A. R. Rocha, V. M. García-Suárez, S. W. Bailey, C. J. Lambert, J. Ferrerand, S. Sanvito, *Nat. Mater.* **2005**, 4, 335-339; c) M. Ganzhorn, S. Klyatskaya, M. Ruben, W. Wernsdorfer, *Nature Nanotech.* **2013**, 8, 165-169.

[3] a) F. Troiani, M. Affronte, *Chem. Soc. Rev.* **2011**, 40, 3119-3129; b) P. C. E. Stamp, A. Gaita-Ariño, *J. Mater. Chem.* **2009**, 19, 1718-1730; c) M. N. Leuenberger, D. Loss, *Nature* **2001**, 410, 789-793. d) M. Jenkins, T. Hümmer, M. J. Marínez-Pérez, J. García-Ripoll, D. Zueco, F. Luis, *New. J. Physics*, **2013**, 15, 095007-095030.

[4] a) D. N. Woodruff, R. E. P. Winpenny, R. A. Layfield, *Chem. Rev.* **2013**, 113, 5110-5148 and references therein; b) S. Das, A. Dey, S. Biswas, E. Colacio, V. Chandrasekhar, *Inorg. Chem.* **2014**, 53, 3417-3426; c) V. Chandrasekhar, S. Das, A. Dey, S. Hossain, J.-P. Sutter, *Inorg. Chem.* **2013**, 52, 11956-11965; d) D. I. Alexandropoulos, A. Fournet, L. Cunha-Silva, A. M. Mowson, V. Bekiari, G. Christou, T. C. Stamatatos, *Inorg. Chem.* **2014**, 53, 5420-5422; e) J. J. L. Roy, L. Ungur, I. Korobkov, L. F. Chibotaru, M. Murugesu, *J. Am. Chem. Soc.* **2014**, 136, 8003-8010; f) S. Das, S. Hossain, A. Dey, S. Biswas, J.-P. Sutter, V. Chandrasekhar, *Inorg. Chem.* **2014**, 53, 5020; g) M. M. Hänninen, A. J. Mota, D. Aravena, E. Ruiz, R. Sillanpää, A. Camón, M. Evangelisti, E. Colacio, *Chem. Eur. J.* **2014**, 20, 8410-8420; h) D. I. Alexandropoulos, L. Cunha-Silva, L. Pham, V. Bekiari, G. Christou, T. C. Stamatatos, *Inorg. Chem.* **2014**, 53, 3220-3229; i) R. McLellan, M. A. Palacios, C. M. Beavers, S. J. Teat, E. K. Brechin, S. J. Dalgarno, *Chem. Commun.* **2013**, 49, 9552-9554; j) F. Habib, M. Murugesu, *Chem. Soc. Rev.* **2013**, 42, 3278-3288 and references therein; k) P. Zhang, Y.-N. Guo, J.

Tang, *Coord. Chem. Rev.* **2013**, 257, 1728; l) R. A. Layfield, *Organometallic* **2014**, 33, 1084-1099; m) S.-Y. Lin, J. Tang, *Polyhedron* **2014**, DOI: 10.1016/j.poly.2014.06.013.

[5] a) D. Gatteschi, R. Sessoli, J. Villain, *Molecular Nanomagnets*; Oxford University Press: Oxford, U. K., **2006**; b) L. Sorace, C. Benelli, D. Gatteschi, *Chem. Soc. Rev.* **2012**, 42, 3278-3288; c) J. D. Rinehart, J. R. Long, *Chem. Sci.* **2011**, 2, 2078-2085; (d) J. J. Baldoví, S. Cardona-Serra, J. M. Clemente-Juan, E. Coronado, A. Gaita-Ariño, A. Pali, *Inorg. Chem.* **2012**, 51, 12565-12574.

[6] a) K. R. Meihaus, J. D. Rinehart, J. R. Long, *Inorg. Chem.* **2011**, 50, 8484-8489; b) F. Habib, P.-H. Lin, J. Long, I. Korobkov, W. Wernsdorfer, M. Murugesu, *J. Am. Chem. Soc.* **2011**, 133, 8830-8833; c) S. Titos-Padilla, J. Ruiz, J. M. Herrera, E. K. Brechin, W. Wernsdorfer, F. Lloret, E. Colacio, *Inorg. Chem.* **2013**, 52, 9620-9626; d) F. Habib, P.-H. Lin, J. Long, I. Korobkov, W. Wernsdorfer, M. Murugesu, *J. Am. Chem. Soc.* **2011**, 133, 8830-8833.

[7] a) J. Ruiz, A. J. Mota, A. Rodríguez-Diéguez, S. Titos, J. M. Herrera, E. Ruiz, E. Cremades, J. P. Costes, E. Colacio, *Chem. Commun.* **2012**, 48, 7916-7918; b) M. A. Palacios, S. Titos-Padilla, J. Ruiz, J. M. Herrera, S. J. A. Pope, E. K. Brechin, E. Colacio, *Inorg. Chem.* **2014**, 53, 1465-1474; c) P.-H. Lin, W.-B. Sun, Y.-M. Tian, P.-F. Yan, L. Ungur, L. F. Chibotaru, M. Murugesu, *Dalton Trans.* **2012**, 41, 12349-12352.

[8] a) S. Das, A. Dey, S. Kundu, S. Biswas, A. J. Mota, E. Colacio, V. Chandrasekhar, *Chem. Asian. J.* **2014**, 9, 1876-1887; b) V. Chandrasekhar, S. Das, A. Dey, S. Hossain, S. Kundu, E. Colacio, *Eur. J. Inorg. Chem.* **2014**, 397-406; c) E. Colacio, J. Ruiz, A. J. Mota, M. A. Palacios, E. Cremades, E. Ruiz, F. J. White, E. K. Brechin, *Inorg. Chem.* **2012**, 51, 5857-5868; d) E. Colacio, J. Ruiz, A. J. Mota, M. A. Palacios, E. Ruiz, E. Cremades, M. M. Hänninen, R. Sillanpää, E. K. Brechin, *C. R. Chim.* **2012**, 15, 878-888; e) E. Colacio, J. Ruiz, E. Ruiz, E.

Cremades, J. Krzystek, S. Carretta, J. Cano, T. Guidi, W. Wernsdorfer, E. K. Brechin, *Angew. Chem. Int. Ed.* **2013**, *52*, 9130-9134.

[9] a) A. Watanabe, A. Yamashita, M. Nakano, T. Yamamura, T. Kajiware, *Chem. Eur. J.* **2011**, *17*, 7428-7432; b) A. Bhunia, M. T. Gamer, L. Ungur, L. F. Chibotaru, A. K. Powell, Y. Lan, P. W. Roesky, F. Menges, C. Riehn, G. Niedner-Schatteburg, *Inorg. Chem.* **2012**, *51*, 9589-9597.

[10] a) A. Yamashita, A. Watanabe, S. Akine, T. Nabeshima, M. Nakano, T. Yamamura, T. Kajiware, *Angew. Chem. Int. Ed.* **2011**, *50*, 4016-4019; b) S. K. Langley, N. F. Chilton, B. Moubaraki, K. S. Murray, *Chem. Commun.* **2013**, *49*, 6965-6967; c) L. Zhao, J. Wu, S. Xue, J. Tang, *Chem. Asian J.* **2012**, *7*, 2419-2423; d) S. K. Langley, N. F. Chilton, B. Moubaraki, K. S. Murray, *Inorg. Chem.* **2013**, *52*, 7183-7192; e) T. Kajiware, M. Nakano, K. Takahashi, S. Takaishi, M. Yamashita, *Chem. Eur. J.* **2011**, *17*, 196-205; f) J.-L. Liu, Y.-C. Chen, Y.-Z. Lin, W.-Q. Zheng, L. Ungur, W. Wernsdorfer, L. F. Chibotaru, M.-L. Tong, *Chem. Sci.* **2013**, *4*, 3310-3316; g) I. Oyarzabal, J. Ruiz, J. M. Seco, M. Evangelisti, A. Camón, E. Ruiz, D. Aravena, E. Colacio, *Chem. Eur. J.* **2014**, *20*, 14262-14269 h) A. Upadhyay, S. K. Singh, C. Das, R. Mondol, S. K. Langley, K. S. Murray, G. Rajaraman, M. Shanmugam, *Chem. Commun.* **2014**, *50*, 8838-8841.

[11] a) J. C. G. Bünzli, S. V. Eliseeva, *Chem. Sci.* **2013**, *4*, 1939-1949. b) S. V. Eliseeva, J. C. G. Bünzli, *Chem. Soc. Rev.* **2010**, *39*, 189-227. c) C. M. G. Santos, A. J. Harte, S. J. Quinn, T. Gunnlaugsson, *Coord. Chem. Rev.* **2008**, *252*, 2512-2527. d) N. Weibel, L. Charbonnière, M. Guardigli, A. Roda, R. Ziessel, *J. Am. Chem. Soc.* **2004**, *126*, 4888-4896.

[12] a) L. Armelao, S. Quici, F. Barigelletti, G. Accorsi, G. Bottaro, M. Cavazzini, E. Tondello, *Coord. Chem. Rev.* **2010**, *254*, 487-505; b) J. D. B. Bradley, M. Pollnau, *Laser Photonics Rev.*

2011, 5, 368-403; c) A. de Bettencourt-Dias, *Dalton Trans.* **2007**, 2229-2241. d) M. A. Katkova, M. N. Bochkarev, *Dalton Trans.* **2010**, 39, 6599-6612.

[13] a) B. H. Bakker, M. Goes, N. Hoebe, H. J. Van Ramesdonk, J. W. Verhoeven, M. H. V. Werts, J. W. Hofstraat, *Coord. Chem. Rev.* **2000**, 208, 3-16; b) S. I. Klink, H. Keizer, F. C. J. M. van Veggel, *Angew. Chem. Int. Ed.* **2000**, 39, 4319-4321; c) G. L. Law, T. A. Pham, J. Xu, K. N. Raymond, *Angew. Chem. Int. Ed.* **2012**, 51, 2371-2374.

[14] W. T. Carnall, The Absorption and Fluorescence Spectra of Rare Earth Ions in Solution. In *Handbook on the Physics and Chemistry of Rare Earths*; Gschneidner, K. A., Jr., Eyring, L., Eds.; North Holland Publishing, Co.: Amsterdam, The Netherlands, **1979**, 3, 172.

[15] (a) S. I. Weissman, *J. Chem. Phys.* **1942**, 10, 214-217; b) J.-C. G. Bünzli, C. Piguet, *Chem. Soc. Rev.* **2005**, 34, 1048-1077; c) N. Chatterton, Y. Bretonniere, J. Pecaut, M. Mazzanti, *Angew. Chem. Int. Ed.* **2005**, 44, 7595-7598. d) F. Pointillart, B. Le Guennic; S. Golhen; O. Cador; O. Maury; L. Ouahab, *Chem. Commun.*, **2013**, 49, 615-617. e) Q.-W. Li, J.-L. Liu, J.-H. Jia, J.-D. Leng, W.-Q. Lin, Y.-C. Chen, M.-L. Tong, *Dalton Trans.* **2013**, 42, 11262-11270.

[16] a) M. Sakamoto, K. Manseki, H. Okawa, *Coord. Chem. Rev.* **2001**, 219, 379-414; b) N. M. Shavaleev, L. P. Moorcraft, S. J. A. Pope, Z. R. Bell, S. Faulkner, M. D. Ward, *Chem. Eur. J.* **2003**, 9, 5283-5291; c) Y.-Q. Sun, J. Zhang, G.-Y. Yang, *Chem. Commun.* **2006**, 4700-4702; d) S.-L. Zheng, X.-M. Chen, *Aust. J. Chem.* **2004**, 57, 703-712; e) S. Torelli, D. Imbert, M. Cantuel, G. Bernardinelli, S. Delahaye, A. Hauser, J.-C. G. Bünzli, C. Piguet, *Chem. Eur. J.* **2005**, 11, 3228-3242; f) P. B. Glover, P. R. Ashton, L. J. Childs, A. Rodger, M. Kercher, R. M. Williams, L. De Cola, Z. Pikramenou, *J. Am. Chem. Soc.* **2003**, 125, 9918-9919; g) S. M. T. Abtab, A. Audhya, N. Kundu, S. K. Samanta, P. S. Sardar, R. J. Butcher, S. Ghosh, M. Chaudhury, *Dalton*

Trans. **2013**, *42*, 1848-1861; h) T. D. Pasatoiu, C. Tiseanu, A. M. Madalan, B. Jurca, C. Duhayon, J. P. Sutter, M. Andruh, *Inorg. Chem.* **2011**, *50*, 5879-5889.

[17] V. Chandrasekhar, R. Azhakar, J. F. Bickley, A. Steiner, *Chem. Commun.* **2005**, 459-461.

[18] a) V. Chandrasekhar, P. Bag, B. Murugesapandian, M. D. Pandey, *Dalton Trans.* **2013**, *42*, 15447-15456; b) V. Chandrasekhar, B. M. Pandian, *Acc. Chem. Res.* **2009**, *42*, 1047-1062; c) V. Chandrasekhar, B. M. Pandian, R. Boomishankar, A. Steiner, J. J. Vittal, A. Hourri, R. Clérac, *Inorg. Chem.* **2008**, *47*, 4918-4929; d) V. Chandrasekhar, B. M. Pandian, R. Boomishankar, A. Steiner, R. Clérac, *Dalton Trans.* **2008**, *38*, 5143-5145; e) V. Chandrasekhar, B. M. Pandian, J. J. Vittal, R. Clérac, *Inorg. Chem.* **2009**, *48*, 1148-1157; f) V. Chandrasekhar, B. M. Pandian, R. Azhakar, J. J. Vittal, R. Clerac, *Inorg. Chem.* **2007**, *46*, 5140-5142.

[19] a) M. Llunell, D. Casanova, J. Cirera, J. M. Bofill, P. Alemany, S. Alvarez, M. Pinsky, D. Avnir, D. SHAPE v1.1b, Barcelona, **2005**; b) A. Ruiz-Martínez, D. Casanova, S. Alvarez, *Chem. Eur. J.* **2008**, *14*, 1291-1303; c) M. Llunell, D. Casanova, J. Cirera, P. Alemany, S. Alvarez, SHAPE: Program for the stereochemical analysis of molecular fragments by means of continuous shape measures and associated tools; University of Barcelona, Barcelona, Spain, **2010**.

[20] a) H. L. C. Feltham, Y. Lan, F. Klöwer, L. Ungur, L. F. Chibotaru, A. K. Powell, S. Brooker, *Chem. Eur. J.* **2011**, *17*, 4362-4365; b) Y. Bi, Y.-N. Guo, L. Zhao, Y. Guo, S.-Y. Lin, S. D. Jiang, J. Tang, B. W. Wang, S. Gao, *Chem. Eur. J.* **2011**, *17*, 12476-12481 and references therein.

[21] D. Aravena, E. Ruiz, *Inorg. Chem.* **2013**, *52*, 13770-13778.

[22] a) J. L. Liu; K. Yuan; J. D. Leng ; L- Ungur.; W. Wernsdorfer; F. S. Guo.; L- F. Chibotaru; M. L. Tong *Inorg Chem.* **2012**, *51*, 8538; b) E. Lucaccini, L. Sorace, M. Perfetti, J.-

- P. Costes, R. Sessoli, *Chem. Commun.*, **2014**, 50, 1648—1651; c) J. Ruiz, G. Lorusso, M. Evangelisti, E. K. Brechin, S. J. A. Pope, E. Colacio, *Inorg. Chem.* **2014**, 53, 3586-94, d) J. M. Zadrozny, M. Atanasov, A. M. Bryan, C.-Y. Lin, B. D. Rekker, P.P. Power, F. Neese, J. R. Long, *Chem. Sci.* **2013**, 4, 125-138.
- [23] R. J. Blagg, L. Ungur, F. Tuna, J. Speak, P. Comar, D. Collison, W. Wernsdorfer, E. J. L. McInnes, L. F. Chibotaru, R. E. P. Winpenny, *Nature Chem.* **2013**, 5, 673-678.
- [24] F. Aquilante, L. De Vico, N. Ferre, G. Ghigo, P. A. Malmqvist, P. Neogady, T. B. Pedersen, M. Pitonak, M. Reiher, B. O. Roos, L. Serrano-Andres, M. Urban, V. Veryazov, R. Lindh, *J. Comput. Chem.* **2010**, 31, 224-247.
- [25] N.F. Chilton, D. Collinson, E. J. L. McInnes, R. E. P. Winpenny, A. Soncini, *Nat. Commun.* **2013**, 4, 2551.
- [26] S. K. Singh, T. Gupta, M. Shanmugam, G. Rajaraman, *Chem. Commun.* **2014**, 50, 15513-15516.
- [27] S. Sivakumar, M. L. P. Reddy, A. H. Cowley, K. V. Vasudevan, *Dalton Trans.* **2010**, 39, 776-786.
- [28] F. J. Steemers, W. Verboom, D. N. Reinhoudt, E. B. Van der Tol, J. W. Verhoeven, *J. Am. Chem. Soc.* **1995**, 117, 9408-9414.
- [29] a) G. H. Dieke, *Spectra and Energy levels of Rare Earth Ions in Crystals*, Interscience, New York, **1968**; b) S. Raphael, M. L. P. Reddy, A. H. Cowley, M. Findlater, *Eur. J. Inorg. Chem.* **2008**, 4387-4394; c) S. Biju, M. L. P. Reddy, A. H. Cowley, K. V. Vasudevan, *J. Mater. Chem.* **2009**, 19, 5179-5187.

- [30] a) N. M. Shavaleev, S. V. Eliseeva, R. Scopelliti, J.-C. G. Bunzli, *Inorg. Chem.* **2010**, *49*, 3927-3936; b) S. Sivakumar, M. L. Reddy, A. H. Cowley, R. R. Butorac, *Inorg. Chem.* **2011**, *50*, 4882-4891.
- [31] a) N. Sabbatini, M. Guardiglia, J. M. Lehn, *Coord. Chem. Rev.* **1993**, *123*, 201-228; b) A. Dossing, *Eur. J. Inorg. Chem.* **2005**, *8*, 1425-1434; c) A. Beeby, I. M. Clarkson, R. S. Dickins, S. Faulkner, D. Parker, L. Royle, A. S. de Sousa, J. A. G. Williams, M. Woods, *J. Chem. Soc. Perkin Trans.* **1999**, *3*, 493-503; d) I. Nasso, S. Bedel, C. Galaup, C. Picard, *Eur. J. Inorg. Chem.* **2008**, 2064-2074.
- [32] B. S. Furniss, A. J. Hannaford, P. W. G. Smith, A. R. Tatchell, *Vogel's Textbook of Practical Organic Chemistry*, 5th ed.; ELBS, Longman: London, **1989**.
- [33] J. C. de Mello, H. F. Wittmann, R. H. Friend, *Adv. Mater* **1997**, *9*, 230-232.
- [34] a) *SMART & SAINT Software Reference manuals*, Version 6.45; Bruker Analytical X-ray Systems, Inc.: Madison, WI, **2003**; b) G. M. Sheldrick, SADABS, *a software for empirical absorption correction*, Ver. 2.05; University of Göttingen: Göttingen, Germany, **2002**; c) *SHELXTL Reference Manual*, Ver. 6.1; Bruker Analytical X-ray Systems, Inc.: Madison, WI, **2000**; d) G. M. Sheldrick, *SHELXTL*, Ver. 6.12; Bruker AXS Inc.: Madison, WI, **2001**; e) G. M. Sheldrick, *SHELXL97, Program for Crystal Structure Refinement*; University of Göttingen: Göttingen, Germany, **1997**; f) K. Brandenburg, *Diamond*, Ver. 3.1eM; Crystal Impact GbR: Bonn, Germany, **2005**.
- [35] M. J. Frisch, G. W. Trucks, H. B. Schlegel, G. E. Scuseria, M. A. Robb, J. R. Cheeseman, G. Scalmani, V. Barone, B. Mennucci, G. A. Petersson, H. Nakatsuji, M. Caricato, X. Li, H. P. Hratchian, A. F. Izmaylov, J. Bloino, G. Zheng, J. L. Sonnenberg, M. Hada, M. Ehara, K. Toyota, R. Fukuda, J. Hasegawa, M. Ishida, T. Nakajima, Y. Honda, O. Kitao, H. Nakai, T.

Vreven, J., J. A. Montgomery, J. E. Peralta, F. Ogliaro, M. Bearpark, J. J. Heyd, E. Brothers, K. N. Kudin, V. N. Staroverov, R. Kobayashi, J. Normand, K. Raghavachari, A. Rendell, J. C. Burant, S. S. Iyengar, J. Tomasi, M. Cossi, N. Rega, N. J. Millam, M. Klene, J. E. Knox, J. B. Cross, V. Bakken, C. Adamo, J. Jaramillo, R. Gomperts, R. E. Stratmann, O. Yazyev, A. J. Austin, R. Cammi, C. Pomelli, J. W. Ochterski, R. L. Martin, K. Morokuma, V. G. Zakrzewski, G. A. Voth, P. Salvador, J. J. Dannenberg, S. Dapprich, A. D. Daniels, Ö. Farkas, J. B. Foresman, J. V. Ortiz, J. Cioslowski, D. J. Fox, Gaussian09; Gaussian: Wallingford, CT, **2009**.

Table of Contents

The sequential reaction of multidentate Schiff base ligand, LH₄ with lanthanide(III) nitrate salts and Zn(NO₃)₃·6H₂O/ Mg(NO₃)₃·6H₂O followed by addition of triethylamine lead to formation of series of linear trinuclear bimetallic complexes containing M₂Ln (M_{II} = Zn/Mg; Ln_{III} = Dy, Gd and Tb) metallic framework. Detailed magnetochemical analysis revealed the single-molecule magnet behaviour in the both Dy(III) derivatives. Also detailed photophysical measurements exhibit metal centered luminescence of the Tb(III) derivatives.

